Atmospheric
Measurement
Techniques
Open Access
Discussions

Nitrogen dioxide observations from the Geostationary Trace gas and Aerosol Sensor Optimization (GeoTASO) airborne instrument: retrieval algorithm and measurements during DISCOVER-AQ Texas 2013

C. R. Nowlan[1], X. Liu[1], J. W. Leitch[2], K. Chance[1], G. González Abad[1], C. Liu[1,a], P. Zoogman[1], J. Cole[2], T. Delker[2], W. Good[2], F. Murcray[2], L. Ruppert[2], D. Soo[2], M. B. Follette-Cook[3,4], S. J. Janz[4], M. G. Kowalewski[4], C. P. Loughner[4,5], K. E. Pickering[4], J. R. Herman[6], M. R. Beaver[7], R. W. Long[7], J. J. Szykman[7], L. M. Judd[8], P. Kelley[5,9], W. T. Luke[9], X. Ren[5,9], and J. A. Al-Saadi[10]

[1]Harvard-Smithsonian Center for Astrophysics, Cambridge, MA 02138, USA
[2]Ball Aerospace & Technologies Corporation, Boulder, CO 80301, USA
[3]Morgan State University/GESTAR, Baltimore, MD 21251, USA
[4]NASA Goddard Space Flight Center, Greenbelt, MD 20771, USA

AMTD

8, 13099–13155, 2015

NO$_2$ retrievals from GeoTASO

C. R. Nowlan et al.

Title Page

Abstract | Introduction

Conclusions | References

Tables | Figures

◄ | ►

◄ | ►

Back | Close

Full Screen / Esc

Printer-friendly Version

Interactive Discussion

[5]University of Maryland, College Park, MD 20742, USA
[6]University of Maryland, Baltimore County, Baltimore, MD 21201, USA
[7]Environmental Protection Agency, Research Triangle Park, NC 27711, USA
[8]University of Houston, Houston, TX 77004, USA
[9]NOAA Air Resources Laboratory, College Park, MD 20740, USA
[10]NASA Langley Research Center, Hampton, VA 23681, USA
[a]now at: University of Science and Technology, Hefei, Anhui, China

Correspondence to: C. R. Nowlan (cnowlan@cfa.harvard.edu)

Title Page

Abstract | Introduction

Conclusions | References

Tables | Figures

|◄ | ►|

◄ | ►

Back | Close

Full Screen / Esc

Printer-friendly Version

Interactive Discussion

C. R. Nowlan et al.

Abstract

The Geostationary Trace gas and Aerosol Sensor Optimization (GeoTASO) airborne instrument is a testbed for upcoming air quality satellite instruments that will measure backscattered ultraviolet, visible and near-infrared light from geostationary orbit. Geo-TASO flew on the NASA Falcon aircraft in its first intensive field measurement campaign during the Deriving Information on Surface Conditions from Column and Vertically Resolved Observations Relevant to Air Quality (DISCOVER-AQ) Earth Venture Mission over Houston, Texas in September 2013. Measurements of backscattered solar radiation between 420–465 nm collected on four days during the campaign are used to determine slant column amounts of NO$_2$ at 250 m × 250 m spatial resolution with a fitting precision of 2.2×10^{15} molecules cm^{-2}. These slant columns are converted to tropospheric NO$_2$ vertical columns using a radiative transfer model and trace gas profiles from the Community Multiscale Air Quality (CMAQ) model. Total column NO$_2$ from GeoTASO is well correlated with ground-based Pandora observations ($r = 0.90$ on the most polluted and cloud-free day of measurements), with GeoTASO NO$_2$ slightly higher for the most polluted observations. Surface NO$_2$ mixing ratios inferred from GeoTASO using the CMAQ model show good correlation with NO$_2$ measured in situ at the surface during the campaign ($r = 0.91$ for the most polluted day). NO$_2$ slant columns from GeoTASO also agree well with preliminary retrievals from the GEO-CAPE Airborne Simulator (GCAS) which flew on the NASA King Air B200 ($r = 0.84$, slope = 0.94). Enhanced NO$_2$ is resolvable over areas of traffic NO$_x$ emissions and near individual petrochemical facilities.

1 Introduction

The next generation of satellite instruments designed for air quality applications will operate from geostationary orbit, providing measurements of trace gases in the Earth's atmosphere with unprecedented spatial and temporal resolution. These instruments in-

clude the upcoming Tropospheric Emissions: Monitoring of POllution (TEMPO) instrument (Chance et al., 2013), which is a component of the NASA decadal survey mission GEOstationary Coastal and Air Pollution Events (GEO-CAPE) (Fishman et al., 2012), the Geostationary Environmental Monitoring Spectrometer (GEMS) (Kim, 2012) and

5   the Sentinel-4 mission (Ingmann et al., 2012), which will focus respectively on North America, East Asia, and Europe and North Africa.

One of the principal trace gas products of these instruments is nitrogen dioxide (NO$_2$). Nitrogen oxides (NO$_x$ ≡ NO + NO$_2$) play a central role in atmospheric air quality. NO$_2$ is a toxic gas, and NO$_x$ is involved in aerosol production and ozone photochem-

10 istry. Globally, the major sources of NO$_x$ are combustion (primarily from transportation and thermal power plants), soils and lightning. In urban areas, sources of NO$_x$ are dominated by transportation and industry, with NO$_2$ showing a strong correlation with total population (Lamsal et al., 2013).

NO$_2$ has relatively strong spectral absorption features in the visible region of the

15 spectrum, which have been exploited over the past two decades for remote sensing using measurements of backscattered solar radiation from several instruments on sun-synchronous satellites (Martin et al., 2002; Boersma et al., 2004; Richter et al., 2011; Bucsela et al., 2013). These instruments are the predecessors of the upcoming geostationary air quality instruments.

20 The Geostationary Trace gas and Aerosol Sensor Optimization (GeoTASO) aircraft instrument (Leitch et al., 2014) has been developed by Ball Aerospace under the NASA Earth Science Technology Office Instrument Incubator Program in support of satellite measurements from geostationary orbit. Originally conceived as a testbed instrument for GEO-CAPE, GeoTASO is now also part of the mission risk reduction for TEMPO

25 and GEMS in both instrument design and retrieval algorithm development.

GeoTASO is able to map the atmosphere in two dimensions (2D) under the aircraft's flight track. GeoTASO operates as a hyperspectral pushbroom scanner, where the spectral information is provided by the y dimension of a 2D CCD array detector, the cross-track spatial dimension is provided by x dimension of the array, and the along-

track spatial dimension is provided by the movement of the aircraft in its flight path. Pushbroom scanner measurements are analogous to the type of measurements that will be made by the geostationary satellite instruments, but the satellite instruments will utilize a scan mirror to move the field-of-view (FOV).

5   These type of measurements from aircraft are relatively new, with pushbroom NO$_2$ airborne 2D measurements reported recently over the Highveld region of South Africa (Heue et al., 2008), Zurich, Switzerland (Popp et al., 2012), northwest Germany (Schönhardt et al., 2014) and Leicester, United Kingdom (Lawrence et al., 2015). General et al. (2014) have also recently reported airborne 2D observations of volcanic BrO and SO$_2$ over Mt. Etna, BrO and NO$_2$ over Alaska, and NO$_2$ over Indianapolis using an instrument equipped with a whiskbroom scanner for nadir observations and a pushbroom scanner observing in limb geometry for obtaining vertical information. In addition, the GEO-CAPE Airborne Simulator (GCAS) (Kowalewski and Janz, 2014) is a recently developed pushbroom sensor which had its first campaign deployment at the same time as GeoTASO.

GeoTASO is also capable of making measurements of O$_3$, SO$_2$ and CH$_2$O in the UV. However, for the particular field campaign on which we focus the current study, the instrument's UV channel suffered from out-of-band stray light. The influence of stray light has been minimized for later flights and work is under way to develop a correction for the Texas flights; however, in the current paper we focus exclusively on NO$_2$.

This paper introduces the GeoTASO instrument and describes algorithm development and the first trace gas retrievals of NO$_2$ from this new instrument. Section 2 describes the GeoTASO optical design and measurement strategy. Section 3 describes the deployment of GeoTASO during the Deriving Information on Surface Conditions from Column and Vertically Resolved Observations Relevant to Air Quality (DISCOVER-AQ) Texas 2013 field campaign and introduces supporting measurements for validation. Section 4 describes the data analysis for GeoTASO observations including calibration and spectral fitting for the retrieval of trace gas amounts. Section 5 presents the first results from GeoTASO and validation using data from other in-

struments collected during the DISCOVER-AQ campaign. Section 6 summarizes the current status of GeoTASO and presents plans for future data analysis.

2 GeoTASO instrument

GeoTASO (Leitch et al., 2014) is a hyperspectral instrument measuring nadir backscattered light in the ultraviolet, visible and near-infrared in two channels at wavelengths 290–400 nm (UV) and 415–695 nm (visible/near-infrared). The main characteristics of the instrument are summarized in Table 1.

2.1 Spectrometer design

GeoTASO uses an Offner imaging spectrometer with the optical design shown in Fig. 1. Light is provided to the spectrometer by a wide-field telescope with an FOV of about 45° in the aircraft's cross-track dimension. After passing through a slit and depolarization assembly, light is reflected and diffracted off mirrors and a grating. A dichroic beamsplitter splits the diffracted light into first (VIS channel) and second (UV channel) orders, which are detected by two 2D CCD detector arrays. Additional blocking filters in the two spectral channels remove any remaining out-of-band light. The CCD arrays each consist of 1024×1024 active individual detector pixels. The slit image is slightly smaller than the full array to allow for slight image shifting and to facilitate initial alignment, so that only the central 975 pixels in the cross-track dimension are well-illuminated in nadir observations. In the wavelength dimension, the image covers 740 pixels on the UV detector and 1000 pixels on the visible detector.

The GeoTASO instrument has been designed to use a reconfigurable slit and depolarization assembly for testing the sensitivity of trace gas retrievals to changing passband, spectral sampling and polarization. The 13-mm-long slit can be replaced manually, in a precision-registered slit holder that maintains instrument alignment, by slits of various widths (26.0, 32.5, 39.0 and 45.5 µm). A pair of electronically-controlled pho-

toelastic modulators (PEMs) positioned before and after the slit serve as a depolarizer (Illing, 2009) that can be turned off and on or adjusted to optimize depolarization at particular wavelengths during the flight.

The spectrometer and telescope are contained within a thermally-stabilized housing which is mounted kinematically to the aircraft. On the NASA HU-25C Falcon aircraft, the instrument is mounted to the seat rails and the telescope looks at the nadir direction through a fused silica window on the bottom of the aircraft.

2.2 Measurement strategy

Figure 2 shows the geometry of the GeoTASO observations. At a typical flight altitude of 11 km above the surface, the 45° FOV results in a cross-track FOV of 9.1 km for the full field. This results in a cross-track instantaneous FOV (IFOV) of approximately 9 m for each spatial sample. The along-track IFOV is determined by the product of the detector integration time of 0.25 s and the aircraft ground speed, with some variation due to aircraft pitch. At typical aircraft ground speed ($\sim$200 m s^{-1}) and pitch, the along-track IFOV is on the order of 50–80 m.

Nadir measurements are typically interspersed with manually-commanded zenith sky reference and dark current observations. GeoTASO collects zenith observations through an optical fiber bundle that looks out the top of the aircraft. As a result, the zenith spectra fill only the center of the FOV and are detected with sufficient signal for analysis over about 60 pixels in the cross-track dimension. A typical zenith-sky measurement sequence collects about 580 such observations, resulting in approximately 35 000 individual spectra per zenith sequence. Zenith sky spectra are co-added to improve signal-to-noise as described in Sect. 4.2. Dark current observations are also collected periodically by commanding the closure of shutters immediately in front of the CCD arrays.

NO$_2$ retrievals from GeoTASO

C. R. Nowlan et al.

Title Page

Abstract	Introduction
Conclusions	References
Tables	Figures

|◄ | ►|
◄ | ►

Back | Close

Full Screen / Esc

Printer-friendly Version

Interactive Discussion

3   DISCOVER-AQ campaign

DISCOVER-AQ was a NASA Earth Venture suborbital class mission which involved four field campaigns over four years, aimed at improving the ability of satellite observations to be applied for air quality monitoring. As part of the campaigns, instruments on the NASA King Air B200 aircraft (remote sensing observations) and the P-3B aircraft (in situ observations) collected a large suite of trace gas, meteorological and aerosol observations in concert with stationary and mobile ground-based and ship-based remote sensing and in situ monitoring instruments. GeoTASO flew on the NASA HU-25C Falcon aircraft during the DISCOVER-AQ field campaigns in September 2013 (Texas) and July–August 2014 (Colorado).

3.1   GeoTASO measurements during DISCOVER-AQ Texas 2013

During the 2013 campaign, the GeoTASO instrument was based in Southeast Houston at the William P. Hobby Airport and flew seven flights on six days between 12 September and 24 September 2013, including inbound and outbound transits from and to the Falcon's base at NASA Langley Research Center in Virginia. These flights are summarized in Table 2, along with the slit size used for each flight. The inbound transit from Virginia included observations near Atlanta, Georgia close to large power plants. The 16 September flight made a direct underpass of the Aura satellite as it passed over southern Oklahoma. This flight was made with the intention to compare with retrievals from the Ozone Monitoring Instrument (OMI) on Aura; although OMI NO$_2$ measurements on that day over Texas and Oklahoma were below the detection limit, GeoTASO was able to detect NO$_2$ over Forth Worth, Texas. The 17 September observations were made primarily over water, in support of the ocean color segment of the GEO-CAPE mission, which aims to derive chlorophyll fluorescence and water-leaving radiances in the near-UV, visible and near-infrared from geostationary orbit. The 13, 14, 18 and 24 (Leg 1) September flights occurred over the greater Houston area and enabled observations of pollution from industrial and urban transportation sources. Leg 2 of the 24

September flights passed over three large power plants in North Carolina during the aircraft's transit back to Virginia. In this paper, we examine data from the Houston urban flights on 13, 14, 18 and 24 September.

3.2 Additional data sources

In this study, we use NO_2 data from ground, aircraft and satellite-based measurements, as well as model data produced for the campaign. The surface observations are primarily from twelve DISCOVER-AQ campaign sites in the Houston area, which are listed in Table 3 along with the instruments deployed at the sites. Fig. 3 shows the location of these DISCOVER-AQ sites.

3.2.1 Pandora

Total column NO_2 was measured by Pandora spectrometers (Herman et al., 2009) during DISCOVER-AQ Texas by direct sun observation with a temporal resolution of 90 s, a typical precision of 2.7×10^{14} molecules cm^{-2} and an accuracy of 2.7×10^{15} molecules cm^{-2}. Pandora NO_2 is determined from the difference between the direct sun observation and a reference spectrum derived using clean observations on a clear day. Total column NO_2 is derived using NO_2 cross sections at 255 K (Vandaele et al., 1998). We use column NO_2 data from fifteen Pandora instruments deployed at eleven sites coincident with GeoTASO overpasses.

3.2.2 TCEQ SLAMS

The Environmental Protection Agency (EPA) coordinates a series of sites as part of the national State and Local Air Monitoring Stations (SLAMS) and relevant air quality networks which monitor ambient air quality in the United States at rural, suburban and urban locations. In Texas, these are operated by the Texas Commission on Environmental Quality (TCEQ). We use TCEQ SLAMS NO_2 measurements measured by chemiluminescence and reported hourly at eleven sites in the Houston area coincident

with GeoTASO overpasses during DISCOVER-AQ Texas. These include monitors co-located with eight DISCOVER-AQ science sites listed in Table 3. These measurements are made by Federal Reference Method (FRM) chemiluminescence using molybdenum converters and are known to have high measurement biases under certain conditions relative to other observations (Lamsal et al., 2008). The FRM instruments' listed detection limit is 2.7 ppbv.

3.2.3 EPA research instrumentation

The EPA deployed five research instruments measuring NO_2 every 60 s or less at four sites. These included two Cavity Attenuated Phase Shift (CAPS) instruments which measure NO_2 directly by absorption at 450 nm with an uncertainty ±10 %, two chemi-luminescence NO_x analyzers with photolytic converters with an NO_2 uncertainty of ±15 %, and a high-sensitivity FRM chemiluminescence molybdenum converter instrument deployed in tandem with a CAPS instrument.

3.2.4 NOAA instrumentation

A Cavity Ring-Down (CRD) instrument was deployed by the National Oceanic and Atmospheric Administration (NOAA) and University of Maryland at the Manvel Croix science site in south Houston. The CRD instrument measured ambient NO_2 every 10 s with an uncertainty of ±5 %. The instrument was calibrated with a NIST-traceable NO_2 standard as well as the gas phase titration (GPT) method (Brent et al., 2013). A NOAA chemiluminescence photolytic converter monitor was also deployed at the Galveston site and reported measurements every 60 s, with an uncertainty of ±10 %.

3.2.5 University of Houston instrumentation

The University of Houston (UH) made measurements of NO_2 at altitudes of 7 and 70 m at the Moody Tower site in downtown Houston. These were collected with a chemilu-

minescence monitor fitted with a photolytic converter and have a reported uncertainty of ±12 %. Data are reported every 5 min.

3.2.6 GCAS

The GCAS instrument (Kowalewski and Janz, 2014) was deployed on the NASA King Air B200 aircraft as part of the campaign's airborne remote sensing payload, which also included the NASA High Spectral Resolution Lidar (HSRL) instrument (Hair et al., 2008) for aerosol studies. GCAS operates in a similar fashion to GeoTASO, utilizing a 2D CCD array detector to map slant columns of NO_2 in two dimensions. It is a successor to the Airborne Compact Atmospheric Mapper (ACAM) scanning instrument (Liu et al., 2015). The DISCOVER-AQ Texas campaign was the first deployment of GCAS.

3.2.7 GOME-2

The Global Ozone Monitoring Experiment-2 (GOME-2) instruments (Munro et al., 2015) were launched on the EUMETSAT satellites Metop-A in 2006 and Metop-B in 2013. GOME-2 instruments make nadir observations of backscattered solar radiation from 240–790 nm. Only Metop-A data are considered here, as there were no cloud-free coincidences with Metop-B during DISCOVER-AQ Texas. As of mid-2013, the GOME-2/Metop-A nominal pixel resolution is $40 \times 40 \, \text{km}^2$. We use the publicly-available BIRA-IASB/KNMI GOME-2 NO_2 product TM4NO2A version 2.3 (http://www.temis.nl) (Boersma et al., 2004).

3.2.8 CMAQ model

The EPA's Community Multiscale Air Quality (CMAQ) Version 5.0.2 modeling system (Byun and Schere, 2006) was used to simulate air quality from 18 August 2013 through 1 October 2013. CMAQ used offline meteorology from the Advanced Research Weather Research and Forecasting (WRF-ARW) model (Skamarock et al., 2008) via the Meteorology–Chemistry Interface Processor (MCIP) (Otte and Pleim, 2010). This

time period covers the entire DISCOVER-AQ Texas field deployment in September 2013 plus additional days in August to provide adequate model spin-up time. The 36, 12, and 4 km modeling domains are shown in Fig. 4. The 12 km North American Mesoscale (NAM) model was used for meteorological initial and boundary conditions. Observational and analysis nudging were performed on all domains. Observational nudging was done using the National Centers for Environmental Prediction (NCEP) Automated Data Processing (ADP) Global Surface (http://rda.ucar.edu/datasets/ds461.0/) and Upper Air (http://rda.ucar.edu/datasets/ds351.0/) Observational Weather Data.

WRF was run using an iterative technique developed at the EPA (Appel et al., 2014). The initial WRF run performed analysis nudging on all domains based on the 12 km NAM. The second WRF run performed analysis nudging on all domains based on the 12 km NAM except for 2 m temperature and humidity for the 4 km domain, for which 2 m temperature and humidity from the 4 km initial WRF simulation were used for nudging. This modeling technique prevented the relatively coarse NAM 12 km model from degrading the high resolution 4 km domain. The second iterative WRF runs were used to drive the CMAQ simulation. The CMAQ simulation employs 45 vertical levels, extending from the surface to 50 hPa. WRF and CMAQ options are shown in Table 4.

4 Analysis method

The calculation of NO_2 vertical columns is performed using a two-step approach. First, the slant column amount of the gas in the viewing path is retrieved by fitting a modeled spectrum to the ratio of each nadir spectrum to a zenith sky reference spectrum. Then, the slant column is converted to a vertical column of NO_2 using an air mass factor (AMF) that considers viewing geometry and radiative transfer. Pre-processing of the data involves calibration of raw Level 0 spectra to calibrated Level 1B spectra, and calculation of a zenith sky reference spectra.

The GeoTASO retrieval algorithm is based on existing algorithms developed at the Smithsonian Astrophysical Observatory for GOME, GOME-2, OMI and OMPS (Ozone

Mapping and Profiler Suite) trace gas products (e.g., Chance et al., 2000; Nowlan et al., 2011; González Abad et al., 2015a, b), which are also the heritage algorithms for TEMPO trace gas retrievals.

4.1 Calibration

Spectra are converted from detector counts to radiometrically-calibrated spectra using laboratory measurements of sensor wavelength scale and responsivity over the full FOV. Calibrations use an integrating sphere with line or broad spectrum sources. The integrating sphere is referenced to known calibration sources to give an absolute radiance calibration with roughly 10 % uncertainty in the visible. Measurements from pixels outside the imaging area are used in the calibration to remove smear signal and apply a stray light correction. Polarization sensitivity was measured but not included in these preliminary radiance calibrations as it is at a low level (<5 %). The UV channel for the Texas campaign suffered from excess stray light in the shorter wavelengths (290–350 nm), which has been reduced for later campaigns by the addition of a baffle in the spectrometer (Leitch et al., 2014).

The instrument slit functions measured in the laboratory for the four instrument slits indicate their shapes and widths are consistent across both the FOV and wavelength dimensions of the detector arrays (Leitch et al., 2014). The stability of the slit shape with cross-track position and wavelength are confirmed here using flight data by fitting a slit function to nadir spectra as a preliminary step in the trace gas retrievals.

This approach follows a wavelength-dependent slit and wavelength calibration method previously implemented in the retrieval algorithm to determine slit shape and wavelength calibration from GOME (Liu et al., 2005) and GOME-2 (Cai et al., 2012) irradiance spectra using a high resolution solar reference (Chance and Kurucz, 2010), but simultaneously retrieves preliminary trace gas columns and Ring scaling parameters to remove the effects of atmospheric absorption and the Ring effect present in nadir spectra (Liu et al., 2015). We find the slit function is best modeled for the two largest slit sizes in the visible (Table 1) using a hybrid Gaussian and flat-top Gaussian

defined by:

$$F = (1 - w) \exp \left[\frac{-\Delta\lambda^2}{(h(1 \pm a))^2} \right] + w \exp \left[\frac{-\Delta\lambda^4}{(h'(1 \pm a'))^4} \right] \tag{1}$$

where the algorithm simultaneously fits a relative weighting w between the standard and flat-top Gaussian, and terms h (standard) and h' (flat-top), which represent the half-width at $1/e$, and a and a', which represent asymmetry in the Gaussians. For the UV and two smallest slits in the visible, the slit shape is closest approximated by a Gaussian with no flat-top component. These slit shapes are only minimally asymmetric.

Figure 5 shows the slit functions determined using flight data with those measured in the laboratory for the center FOV position. Although only visible trace gas retrievals are performed in this paper, we include the UV calibration for completeness. Laboratory measurements were performed for the 26, 39 and 45.5 µm slit sizes at three field angles and several wavelengths across the array after the campaign. Our retrieved slit shapes are in good agreement with the measured slit functions, indicating that the slit function parameterization and retrieval using nadir data are both valid for the trace gas retrievals. Retrieved full-width at half maxima are noted in Table 1. The FWHM changes by less than 0.015 nm with wavelength and cross-track pixel across the detector array.

A wavelength-to-pixel registration represented by a second-order polynomial is determined for each spectrum using the same method as the slit function calculation using pseudo absorbers, by fitting to a high resolution solar reference (Chance and Kurucz, 2010).

4.2 Zenith sky reference spectra

A mean zenith sky reference spectrum is determined for each nadir observation using the nearest three zenith sky sequences closest in time, which usually occur within 20 min of the nadir observation. The signal-to-noise ratio of the resulting zenith spectrum varies with solar zenith angle and wavelength, but is approximately 1000–2000 in

the NO$_2$ fitting window. In future, averaging could include even more spectra to reduce the influence of zenith noise in the retrievals.

4.3 Spectral fitting

NO$_2$ slant columns are determined from individual spectra at native spatial resolu-
tion between wavelengths 420–465 nm by simultaneously fitting line-of-sight NO$_2$ slant columns and other parameters listed in Table 5. The fit uses NO$_2$ cross sections at 294 K. In addition to NO$_2$, trace gas amounts are simultaneously retrieved for O$_3$ using cross sections at 218 and 295 K, H$_2$O vapor using an effective cross section determined from high resolution absorption lines at 288 K and 1 atm, and the O$_2$–O$_2$ collision com-
plex at 293 K.

The following pseudo-absorbers are also included in the fit: a Ring spectrum that accounts for filling-in of Fraunhofer lines in the solar spectrum due to rotational Ra-
man scattering; undersampling of the spectrum that occurs when spectral sampling is less than $\sim$3 pixels across the FWHM (Chance et al., 2005); and closure and base-
line polynomials to represent low frequency features in the spectrum due to aerosols, molecular scattering, wavelength-dependent albedo and low-order effects that may not be accounted for properly in radiometric calibration. A wavelength shift is also fit to account for the relative difference in wavelength-detector pixel registration between the nadir radiance and reference spectra.

In this study, fitted NO$_2$ slant columns at native spatial resolution are co-added for 27 across-track and 4 along-track pixels to reduce noise in the columns, resulting in an effective spatial footprint at the surface of about 250 m × 250 m. While satellite observations cover large ground footprints (on the order of tens of km), which require the derivation of cloud fractions to ensure large amounts of data are not discarded, the high native spatial resolution of GeoTASO pixels allows the total removal of cloudy observations and only cloud-free data are presented here. Cloudy pixels are removed using a straightforward limit on the mean radiance by filtering for all single frames where the mean radiance in the NO$_2$ fitting window exceeds 2×10^{13} photons cm^2 nm^{-1} s^{-1}.

Title Page

Abstract | Introduction

Conclusions | References

Tables | Figures

◄ | ►

◄ | ►

Back | Close

Full Screen / Esc

Printer-friendly Version

Interactive Discussion

Mean root-mean square (RMS) fitting uncertainties in normalized spectra at native resolution are on the order of 0.01 for bright, cloud-free scenes, and 0.02 for dimmer scenes. The 39 and 45.5 µm slit sizes give the best fitting performance, while RMS fitting errors are larger by 15 % for the 32.5 µm slit and by 30 % for the 26.0 µm slit.

4.4 Cross-track striping

GeoTASO NO_2 slant column retrievals show the artificial cross track striping that is common in many 2D pushbroom sensors (Boersma et al., 2011; Popp et al., 2012). The magnitude of this striping is persistent throughout each flight, with little day-to-day variation except between campaigns when instrument modifications have likely affected radiometric calibration.

To calculate a destriping correction, we determine the daily offset from the estimated NO_2 slant columns from the CMAQ model as a function of cross-track position, using a large number of retrievals over the relatively clean Gulf of Mexico. The details of this calculation using model calculations and air mass factors are described in the next section.

Figure 6a shows the offset determined from one million spectra on 13 September 2013. At native resolution, striping for the Texas campaign can reach a magnitude of $\pm 4 \times 10^{16}$ molecules cm^{-2} but is typically on the order of $\pm 9 \times 10^{15}$ molecules cm^{-2}. Figs. 6b and 6c show the effects of the striping and corrected columns at 250 m × 250 m resolution for a clear region over water. At co-added resolution, the striping is reduced in magnitude, with individual stripes occasionally as large as $\pm 5 \times 10^{15}$ molecules cm^{-2}. The application of the striping correction removes any evidence of cross-track striping along the entire flight.

4.5 Air mass factor calculation

The conversion of retrieved slant column S to vertical column V requires an air mass factor (AMF) A that describes the vertically resolved contribution of the trace gas, where

$$V = \frac{S}{A}. \tag{2}$$

The magnitude of the AMF depends on the vertical profile of the gas of interest (NO_2), ozone profile, aerosol optical depth, molecular scattering, surface albedo, cloud top pressure and radiative cloud fraction. In the case of the GeoTASO data, the high spatial resolution of native pixel observations allows clouds to be removed from processed data, and all co-added pixels are assumed to be clear-sky. AMFs are calculated here for each local co-added scene following the formulation of Palmer et al. (2001), with scattering weights calculated using the radiative transfer model VLIDORT (Spurr, 2006).

The scattering weights $w(z)$ describe the sensitivity of the measurement to different altitude layers, and can be used with any trace gas profiles in model and instrument comparisons. They are related to the AMF by

$$A = \int_z w(z)s(z)\mathrm{d}z \tag{3}$$

with the shape factor $s(z)$ describing the normalized density $x(z)$ of the trace gas of interest at altitude z:

$$s(z) = \frac{x(z)}{\int_z x(z)\mathrm{d}z}. \tag{4}$$

The surface reflectivity representation in the scattering weight calculation uses bidirectional reflectance distribution functions (BRDF) (Schaaf et al., 2002) determined from the high-resolution (30 arc second) MODIS BRDF MCD43GF V005 Band

NO$_2$ retrievals from GeoTASO

C. R. Nowlan et al.

Title Page

Abstract | Introduction

Conclusions | References

Tables | Figures

◀ | ▶|

◀ | ▶

Back | Close

Full Screen / Esc

Printer-friendly Version

Interactive Discussion

3 product centered at 470 nm (http://www.umb.edu/spectralmass/terra_aqua_modis/modis_brdf_albedo_product_mcd43). We determine the scattering weights and AMF at 470 nm, which is the closest wavelength where MODIS BRDF's are available. Where MODIS BRDF values are not available over water, the surface is represented as Lambertian with an albedo of 0.03.

Tropospheric trace gas profiles are from the CMAQ model at 4 km × 4 km resolution. Stratospheric NO_2 profiles are from a climatology from the PRATMO chemical box model (Prather, 1992; McLinden et al., 2000). A monthly ozone climatology determined from the OMI ozone profile product (Liu et al., 2010) is used in the stratosphere.

The vertical column is determined from the retrieved differential slant column dS, which represents the difference between the nadir slant column S and the reference slant column S_R taken from zenith observations during these flights. In addition, we consider an offset expressed as a slant column S_O to remove striping in the retrieved NO_2 as detailed in Sect. 4.4. The differential slant column is then represented as a function of the slant column below ($S^\downarrow$) and above ($S^\uparrow$) the aircraft by

$$dS = (S^\downarrow + S^\uparrow) - (S_R^\downarrow + S_R^\uparrow) + S_O, \tag{5}$$

with the offset S_O determined from a retrieved differential slant column dS_O retrieved over a relatively clean area of the flight and defined as

$$dS_O = (S_O^\downarrow + S_O^\uparrow) - (S_{R,O}^\downarrow + S_{R,O}^\uparrow) + S_O. \tag{6}$$

By substituting the product of the vertical column and air mass factor for the slant column, we can solve for the vertical column below the aircraft

$$V^\downarrow = \frac{dS - V^\uparrow A^\uparrow + V_R^\downarrow A_R^\downarrow + V_R^\uparrow A_R^\uparrow - S_O}{A^\downarrow} \tag{7}$$

where

$$S_O = dS_O - V_O^\downarrow A_O^\downarrow - V_O^\uparrow A_O^\uparrow + V_{R,O}^\downarrow A_{R,O}^\downarrow + V_{R,O}^\uparrow A_{R,O}^\uparrow \tag{8}$$

For a typical case where measurements are made from a flight altitude of 11 km, $V^{\downarrow}$ and $V^{\uparrow}$ are approximately equivalent to the tropospheric and stratospheric components of the NO$_2$ column, respectively. In these equations, dS and dS_O are determined from the measurements, while the vertical columns and air mass factors are determined us-
ing the modeled atmosphere. In practice, as long as the zenith reference is collected close in time and location to the nadir observation, the terms representing the reference and nadir columns are similar, although they do not cancel entirely. The effect of the column below the aircraft on the zenith observation also tends to be small. Although these terms are considered in these GeoTASO AMF calculations, the observed
differential slant column and the tropospheric air mass factor contribute the majority of the information to the solution.

Figure 7 shows a sample NO$_2$ model profile and scattering weights for a nadir observation over a polluted area of Houston, as well as the profile and scattering weights for a nearby zenith reference spectrum. Similar stratospheric profiles for the nadir and
zenith sky spectra mean that the stratospheric components in Eq. (5) are similar, although the non-zero difference between nadir and zenith scattering weights above the aircraft do indicate that these terms do not entirely cancel. In this illustrated case, $S^{\uparrow} - S_R^{\uparrow} = -5.3 \times 10^{14}$ molecules cm^{-2}. Even though the zenith spectra are often collected over mildly polluted areas during an urban campaign, the small tropospheric
zenith reference scattering weights ensure the zenith contribution from the profile is small, with $S_R^{\downarrow} = 7.6 \times 10^{14}$ molecules cm^{-2} for this particular observation.

4.6 Uncertainties

4.6.1 Slant column uncertainties

The fitting precision of individual NO$_2$ slant column retrievals at native spatial resolution is $\sim 2.3 \times 10^{16}$ molecules cm^{-2}. In this analysis, we present data co-added for 27 across-track and 4 along-track pixels, resulting in an effective spatial resolution of ap-

proximately 250 m × 250 m, with a fitting precision of ∼ 2.2 × 10^{15} molecules cm^{-2} for the differential slant column dS in Eq. (7). This varies with scene brightness over Houston by about ±0.4 × 10^{15} molecules cm^{-2}. The fitting precision is larger in cases where the effective footprint is partially obstructed by a cloud and fewer observations are co-added. For our analysis of high-NO$_2$ regions where NO$_2$ signal dominates over noise, we present data at this spatial resolution as an optimization of spatial resolution and precision; users may improve the effective precision by further spatial co-adding. The GeoTASO design requirement at 1 km × 1 km resolution derived from TEMPO requirements (Chance et al., 2013) is 1 × 10^{15} molecules cm^{-2}; at 1 km × 1 km spatial resolution, the actual precision of 5.5 × 10^{14} molecules cm^{-2} exceeds the requirement.

Additional uncertainties in the differential slant column result from uncertainties in the NO$_2$ measured cross sections of about 2 % (Boersma et al., 2004) and the use of a cross section at a single temperature. Satellite retrievals typically use NO$_2$ cross sections at lower stratospheric temperatures, which can result in uncertainties as high as 20 % in polluted regions if an empirical correction is not applied (Boersma et al., 2004). However, the GeoTASO retrievals use NO$_2$ cross sections at 294 K, and the effect of the colder stratospheric NO$_2$ on the results should be minimized by the use of a zenith sky reference.

The differential slant column correction term dS_O is affected by the same uncertainties in slant column retrievals; however, its effective precision is reduced to 1 × 10^{14} molecules cm^{-2} due to averaging of many spectra in the along-track direction.

4.6.2 Air mass factor and model uncertainties

Uncertainties in air mass factors typically contribute the largest component of satellite vertical column measurement error budgets in polluted observations (Martin et al., 2002; Boersma et al., 2004). Air mass factor uncertainties for cloud-free NO$_2$ data are generally dominated by uncertainties in trace gas vertical profiles, surface reflectivity and aerosols.

The AMF in the NO$_2$ region also has some wavelength dependency, and use of an AMF calculated at a single wavelength can lead to slight biases in the vertical columns. For typical NO$_2$ observations, the effects are small; the AMF varies by about 5 % across the NO$_2$ fitting window between 420 and 465 nm. The AMF at the center of the Geo-TASO fitting window at 442 nm is on the order of 3 % smaller than that at 470 nm (the MODIS BRDF band). In future data processing iterations, we plan to minimize this uncertainty by scaling the high-spatial resolution MODIS BRDF at 470 nm by a lower spatial resolution surface albedo database which contains wavelength-dependent albedo at shorter wavelengths, such as Kleipool et al. (2008).

We estimate an uncertainty of 20 % for MODIS in the BRDF product for both accuracy and precision, based on comparisons between MODIS BRDF derived reflectance and aircraft observations at a similar spatial scale to the GeoTASO 250 m × 250 m observations (Román et al., 2011). The resultant uncertainty in the AMF is about 10 % for polluted scenes and 5 % for clean scenes.

Uncertainties in aerosol distribution can contribute large uncertainties to the AMF, and the presence of aerosols can increase or decrease the AMF, depending on aerosol type (Leitão et al., 2010). When scattering aerosols are located below or at the NO$_2$ layer, the AMF will be enhanced by the increase in observed radiation. In contrast, scattering aerosols located above the layer will obscure NO$_2$ and lower the AMF. Absorbing aerosols above or at the NO$_2$ layer reduce the AMF by removing radiation that would have otherwise returned to the observer.

Recent analysis shows that neglecting high aerosol optical depths (AOD) over China (> 0.8) in the OMI operational retrievals can bias NO$_2$ columns by as much as −40 to 90 % (Lin et al., 2014), in part because of the implicit inclusion of the effects of aerosols in the OMI cloud fraction. The HSRL aerosol lidar on the NASA King Air B200 observed AODs from <0.1–0.7 during DISCOVER-AQ flights coincident with GeoTASO. At these AODs, the biases calculated by Lin et al. (2014) are more typically within ±25 %. Boersma et al. (2004) show that biases in GOME NO$_2$ AMFs from aerosols

near the surface are on the order of 0–7 % (AOD = 0.1) and 4–34 % (AOD = 0.7), depending on aerosol type.

Comparisons between CMAQ and in situ aircraft profiles collected during the campaign from the P-3B aircraft reveal typical uncertainties in profile shape factors on the order of 20 %, which on average result in a ~5 % uncertainty in the AMF below the aircraft. Individual partial column model uncertainties are sometimes much larger (>100 %) when compared with P-3B profiles, which can contribute a small uncertainty through the term $V_R^\downarrow$ in Eq. (7). In addition, we estimate a 30 % uncertainty in NO$_2$ stratospheric columns from the PRATMO model, based on typical differences with OSIRIS limb measurements of NO$_2$ (Bourassa et al., 2011).

Uncertainties in CMAQ surface mixing ratios also directly impact uncertainties in the GeoTASO-inferred surface mixing ratios that will be presented in Sect. 5.2.2. Uncertainties in the model surface estimates vary by time of day and are large in the morning hours. Comparisons between CMAQ surface mixing ratios and the in situ surface NO$_2$ observations during DISCOVER-AQ derived from all sites indicate uncertainties at 9:00 LT are on the order of 6 ppbv, but decrease rapidly by 10:00 LT, with biases <1 ppbv and gross error on the the order of 2 ppbv during the most of the GeoTASO flight times.

5   Results and validation

5.1   Urban NO$_2$ observations

Figure 8 shows NO$_2$ tropospheric vertical columns derived from GeoTASO during four days of DISCOVER-AQ flights over the Houston area. The 13 September was the day with the highest levels of detected NO$_2$ and also the day most free of clouds. An enlarged view of the first overpass of this day over urban Houston is shown in Fig. 9. In these 13 September flights, the two most polluted overpasses occur over downtown Houston and several large freeways (I-10, I-45, I-69, I-610) and their interchanges. The

more southern polluted overpass occurs over the more rural and suburban Route 6, and the Manvel Croix science site. Although there are few local sources of pollution, the suburban Manvel region of Houston regularly has some of the highest ozone concentrations in the Houston area (Sather and Cavender, 2012).

While the majority of NO_2 appears correlated with roads and highly-populated areas, enhanced levels of NO_2 are also detectable over industrial facilities, including those to the east of Houston near the entrance of the Houston ship channel, and the petrochemical manufacturing and petroleum refineries at Texas City on Galveston Bay.

Aerosol optical depths measured by the HSRL lidar on the NASA King Air at 532 nm and by an Aerosol Robotic Network (AERONET) instrument (http://aeronet.gsfc.nasa.gov/) at Moody Tower at 441 nm indicate that maximum aerosol optical depths (AOD) were as large as 0.4 on 13 September and 0.7 on 14 September. HSRL data indicate that a smoke plume present at 2–3 km on the 13th contributed to the larger AOD on this day, and also show significant urban pollution aerosols in the boundary layer. The smoke plume remained on the 14th, but HSRL data indicate that urban pollution aerosols at lower altitudes were the main contributor to the AOD. Aerosol AOD measured during the 18 and 24 September flights was much smaller (<0.15). As discussed in Sect. 4.6.2, the optical properties and vertical distribution of aerosols can have a large influence on the air mass factor.

A full assessment of the effects of aerosols on the GeoTASO NO_2 air mass factors is beyond the scope of this paper; however, a large of amount of aerosol data collected during the DISCOVER-AQ and the concurrent SEAC4RS (Studies of Emissions, Atmospheric Composition, Clouds and Climate Coupling by Regional Surveys) field campaigns over the Southern US is available for a future detailed study on the effects of aerosols on these aircraft retrievals, with results of particular interest when assessed in combination with the independent aerosol retrievals currently under development for GeoTASO (Wang, 2015).

5.2 Urban NO$_2$ comparisons

This section presents comparisons of GeoTASO NO$_2$ with observations made from other instruments during the campaign. Ground-based observations are compared with coincident GeoTASO observations when they fall within GeoTASO's 250 m × 250 m footprint.

5.2.1 Ground-based column observations

Figure 10 shows a comparison between GeoTASO total columns and Pandora total columns measured from the ground. GeoTASO total columns are the sum of the retrieved tropospheric column and the modeled stratospheric column. The stratospheric column is generally on the order of 3×10^{15} molecules cm^{-2} for these observations.

For 13 September, the day when NO$_2$ amounts were most significant over the monitoring stations, we find a good correlation between GeoTASO and Pandora NO$_2$ total column ($r = 0.90$). Correlations are low to fair for the less polluted other days ($r = 0.16 - 0.48$) and increase with increasing pollution, although total columns are relatively small compared to uncertainties. On these cleaner days, the mean bias is within 20 %.

The original 13 September data contain five noticeable measurement outliers, where GeoTASO measures 2–3 times more NO$_2$ than the Pandora spectrometer. Four of these five observations occur at the Moody Tower science site (the fifth is at the Manvel Croix site). At Moody Tower, two Pandora spectrometers observed at an altitude of 70 m from the top of the Moody high-rise towers at the University of Houston. Most of the difference between GeoTASO and uncorrected Pandora columns is due to the resulting missing NO$_2$ partial column in Pandora data below the top of the towers.

In situ observations collected every 5 min by the University of Houston from both the top and base of the tower at a height of 7 m are used here to correct Pandora columns at Moody Tower for the NO$_2$ column below 70 m. For instance, these data indicate that the differential columns below the tower were 8.0×10^{15} molecules cm^{-2} during the first

Title Page

Abstract | Introduction

Conclusions | References

Tables | Figures

|◄ | ►|

◄ | ►

Back | Close

Full Screen / Esc

Printer-friendly Version

Interactive Discussion

GeoTASO overpass and 4.8×10^{15} molecules cm^{-2} during the second on 13 September. When Pandora data are corrected for these missing columns, there is significant improvement in the agreement with GeoTASO total columns. On 13 September, there remains a slight high bias in GeoTASO data relative to Pandora at the highest total
5 columns, which could be due to factors such as different viewing geometry and spatial resolution combined with the spatial inhomogeneity of NO$_2$, instrument vertical sensitivity and air mass factor uncertainties, or stratospheric NO$_2$. Aerosol optical depth is relatively high on this day, with a smoke plume aloft and urban aerosol in the boundary layer, leading to larger uncertainties in the AMF calculation.

10 ### 5.2.2 Surface observations

Of particular interest for satellite missions is the potential to infer surface concentrations from column observations of NO$_2$, which is useful for air quality applications and can be validated using relatively dense in situ data networks. The approach of Lamsal et al. (2008), who inferred OMI surface NO$_2$ using OMI NO$_2$ columns in combination
15 with a chemical transport model, has been used in several applied studies to examine exposure, emission sources, and deposition (Bechle et al., 2013; Lamsal et al., 2013; McLinden et al., 2014; Nowlan et al., 2014), and validated using surface in situ data (Lamsal et al., 2008, 2010, 2015).

We apply this method to infer surface concentrations S_{GT} using GeoTASO NO$_2$ tro-
20 pospheric columns and the CMAQ model profiles. This is done by scaling the lowermost CMAQ surface concentration S_{CMAQ} (∼11 m altitude) by the ratio of the GeoTASO tropospheric column V_{GT} to the CMAQ tropospheric column V_{CMAQ} using

$$S_{GT} = S_{CMAQ} \frac{V_{GT}}{V_{CMAQ}}. \tag{9}$$

Figure 11 shows a comparison of inferred GeoTASO surface concentrations with in
25 situ data collected at the surface, for both the TCEQ SLAMS network and science instruments deployed during the DISCOVER-AQ campaign. The polluted 13 September

day shows very good correlation between the GeoTASO data and both the TCEQ and campaign science instrumentation ($r = 0.89$ and 0.91 respectively). Biases are generally within about 30 %. The agreement is quite good with the Texas Avenue photolytic, Moody Tower photolytic and Manvel Croix CRD instruments, which measure the largest

5   NO_2 concentrations on 13 September.

Several factors can lead to observed differences between GeoTASO and in situ observations, in addition to the uncertainties discussed in Sections 4.6 and 5.2.1. Some high values of the TCEQ data relative to those of GeoTASO may be at least partially explained by the tendency of the FRM NO_2 molybdenum converter measurements to

10   overestimate NO_2. Biases in CMAQ surface concentrations can propagate to Geo-TASO inferred concentrations. On 13 and 24 September, inferred GeoTASO surface concentrations at low ambient NO_2 concentrations are biased low relative to the in situ observations. CMAQ surface concentrations at background levels are similarly biased low relative to the in situ observations on these days, and the bias propagates to the

15   derived GeoTASO surface concentrations. In addition, comparisons may be artificially improved by the fact that the correlation between the model surface concentration and vertical column may be greater than the correlation between the "true" in situ observed concentration at the surface and the profile (observed by the P-3B instruments); Flynn et al. (2014) found that CMAQ profiles during the DISCOVER-AQ Maryland 2011 cam-

20   paign tended to be more well-mixed with altitude than the P-3B profiles. NO_2 temporal variability and inhomogeneity within an aircraft footprint can can also play a large role in uncertainties when aircraft observations are compared with in situ observations at urban locations. For instance, the Moody Tower in situ observations on 18 September varied between 5 and 45 ppbv within 10 min of the second GeoTASO overpass.

25   ### 5.2.3 Aircraft observations

Several NASA Falcon flights were made coincident with the NASA King Air B200 carrying the GCAS instrument during the campaign. Here we present comparisons with preliminary NO_2 retrievals from the GCAS instrument, which was also participating in

its first field campaign since its modifications from the ACAM instrument. Figure 12 shows GCAS (King Air B200 flying at 9 km) and GeoTASO (NASA Falcon flying at 11.3 km) retrieved NO$_2$ slant columns for the first overpass of Houston on 13 September 2013 at the GCAS resolution of 250 m × 500 m. These GeoTASO slant columns correspond to Fig. 8a, before the AMF is applied.

The GCAS retrievals are performed using the GeoTASO fitting algorithm, with identical fitting parameters and wavelength region. The GCAS retrievals use a single mean nadir reference spectrum collected during a pass over the relatively clean Gulf of Mexico. Like GeoTASO, the retrieved GCAS slant columns also showed a persistent background offset. However, in the case of GCAS, we did not find striping as with GeoTASO, but rather that the offset varied smoothly across the field of view from 0 to 1.5 × 10^{16} molecules cm^{-2}. The derived offset is removed from the GCAS slant columns in the data presented in this section.

Figure 13 shows the GCAS and GeoTASO geolocation data and NO$_2$ slant columns averaged across track as a function of local time during the two morning overpasses. The offset in geolocation versus time between the two aircraft is clearly visible in the NO$_2$ peaks. At the beginning of the overpass, GeoTASO was measuring approximately 10 min after GCAS, but just after 10:00 LT the Falcon aircraft overtook the King Air, and the later NO$_2$ observations are shifted by as much as 20 min. Figure 14 shows the GCAS slant column plotted versus its closest GeoTASO coincidence within 10 min and 500 m. The slant columns are well-correlated ($r = 0.84$) and agree well in magnitude, with GeoTASO slant columns on average about 6 % less than GCAS slant columns. The comparison remains similar for tighter coincidence criteria.

On the whole, slant columns between the two instruments agree very well in magnitude, although there are some differences. For instance, in Fig. 12, the southernmost flight legs, which occurred early in the flight (over Manvel Croix, south of downtown Houston), show some differences in NO$_2$ distribution between the two instruments which is likely due to highly variable NO$_2$ and slightly different overpass times. Several local sources are easily detectable in both instruments, including petrochemical manu-

facturing and refining facilities in Texas City and near the Houston Ship Channel. Both instruments show a clear enhancement in NO$_2$ over two large roads (I-10 and Sam Houston Parkway ring road) to the west of Houston's center. Interestingly, although NO$_2$ is still detectable over those roads in the vertical column in Fig. 8, its abundance relative to other areas decreases significantly after the MODIS BRDF has been applied at high spatial resolution, which attempts to account for the effect of surface reflectivity on the retrievals, as these particular highways are flanked by bright buildings bordering darker forests and fields which cause their slant columns to be particularly pronounced relative to their surroundings.

5.2.4 Satellite observations

The only GeoTASO Houston flight that had coincident cloud-free satellite observations was the second Houston overpass on 13 September 2013, which occurred during a GOME-2/Metop-A observation of the Houston area at 11:00 AM LT. (The 14 September flight had a coincident overpass of OMI, but the OMI data are cloudy over the flight area.) Figure 15 shows the GeoTASO NO$_2$ tropospheric column plotted over the $40\,\mathrm{km} \times 40\,\mathrm{km}$ GOME-2 tropospheric columns for this overpass. The precision of these GOME-2 NO$_2$ tropospheric columns is about 1×10^{15} molecules cm^{-2}. A quantitative comparison of the two retrievals is made difficult by the geographic distribution of the GeoTASO data and very different spatial resolutions; however, enhancements in GOME-2 NO$_2$ are consistent with large GeoTASO columns, and mean values are reasonable considering the obvious spatial variability in NO$_2$ within a GOME-2 pixel.

6 Summary and conclusions

We have presented the first trace gas retrieval results from the GeoTASO airborne instrument using data collected during the DISCOVER-AQ field campaign based in Houston, Texas during September 2013. Differential NO$_2$ slant columns are first re-

trieved from the ratio of GeoTASO cloud-free nadir spectra to a mean zenith sky reference spectrum and co-added to 250 m × 250 m resolution after a cross-track striping correction, with a resultant precision of ±2.2 × 10^{15} molecules cm^{-2}. Vertical columns below the aircraft are determined from slant columns using air mass factors derived from a radiative transfer calculation with tropospheric profiles from the CMAQ model and high-resolution MODIS surface BRDF.

Data from the overflights of Houston show good agreement with ground-based observations. Comparisons with total column NO$_2$ measured by ground-based Pandora spectrometers show fair to very good agreement, with $r = 0.16$ for a relatively clean day with little NO$_2$ to $r = 0.90$ for a more polluted day. Little bias is observed except for a slight over-estimation of NO$_2$ by GeoTASO relative to the Pandora instrument at the very highest NO$_2$ columns ($> 2 \times 10^{16}$ molecules cm^{-2}). Surface mixing ratios are also inferred by scaling the ratio of CMAQ-modeled NO$_2$ surface mixing ratios by the ratio of GeoTASO column to the modeled column. These GeoTASO inferred surface mixing ratios correlate well with "true NO$_2$" mixing ratios measured in situ at the surface during the campaign when concentrations are large. Correlations range from $r = 0.49$ for a relatively clean and cloudy day with few coincident polluted in situ observations, to $r = 0.91$ for a polluted day with many coincidences. Correlations with the TCEQ SLAMS network are also quite good ($r = 0.60 - 0.89$). Biases between observations vary by day, but are generally on the order of 30 % for a polluted day.

Preliminary slant column retrievals from the GCAS instrument on the King Air B200 aircraft also agree well in magnitude and distribution with GeoTASO observations taken close in time. We also present an overpass of GOME-2 NO$_2$. Even though direct comparison is difficult with the satellite data due to the geographic distribution of GeoTASO observations, the spatial distribution and magnitude of the NO$_2$ columns are reasonable.

Future work with GeoTASO trace gas retrievals will involve further analysis of Geo-TASO data from the Colorado DISCOVER-AQ campaign, where the instrument flew on a number of flights, as well as validation of other molecules absorbing in the ul-

Title Page

Abstract | Introduction

Conclusions | References

Tables | Figures

|◄ | ►|

◄ | ►

Back | Close

Full Screen / Esc

Printer-friendly Version

Interactive Discussion

traviolet. GeoTASO will also participate as a component of NASA's contribution to the KORUS-AQ air quality field campaign over Korea in 2016.

GeoTASO trace gas products are available from the DISCOVER-AQ data archive at http://www-air.larc.nasa.gov/missions/discover-aq/discover-aq.html.

References

Appel, W., Gilliam, R., Pleim, J., Pouliot, G., Wong, D.-C., Hogrefe, C., Roselle, S., and Mathur, R.: Improvements to the WRF-CMAQ modeling system for fine-scale air quality simulations, EM Magazine, 14 September 2014, 16–21, 2014. 13110

Bechle, M. J., Millet, D. B., and Marshall, J. D.: Remote sensing of exposure to NO_2: Satellite versus ground-based measurement in a large urban area, Atmos. Environ., 69, 345–353, doi:10.1016/j.atmosenv.2012.11.046, 2013. 13123

Boersma, K. F., Eskes, H. J., and Brinksma, E. J.: Error analysis for tropospheric NO_2 retrieval from space, J. Geophys. Res.-Atmos., 109, D04311, doi:10.1029/2003JD003962, 2004. 13102, 13109, 13118, 13119

Boersma, K. F., Eskes, H. J., Dirksen, R. J., van der A, R. J., Veefkind, J. P., Stammes, P., Huijnen, V., Kleipool, Q. L., Sneep, M., Claas, J., Leitão, J., Richter, A., Zhou, Y., and Brunner, D.: An improved tropospheric NO_2 column retrieval algorithm for the Ozone Monitoring Instrument, Atmos. Meas. Tech., 4, 1905–1928, doi:10.5194/amt-4-1905-2011, 2011. 13114

Bourassa, A. E., McLinden, C. A., Sioris, C. E., Brohede, S., Bathgate, A. F., Llewellyn, E. J., and Degenstein, D. A.: Fast NO_2 retrievals from Odin-OSIRIS limb scatter measurements, Atmos. Meas. Tech., 4, 965–972, doi:10.5194/amt-4-965-2011, 2011. 13120

Brent, L., Thorn, W., Gupta, M., Leen, B., Stehr, J., He, H., Arkinson, H., Weinheimer, A., Garland, C., Pusede, S., Wooldridge, P., Cohen, R., and Dickerson, R.: Evaluation of the use of a commercially available cavity ringdown absorption spectrometer for measuring NO_2 in flight, and observations over the Mid-Atlantic States, during DISCOVER-AQ, J. Atmos. Chem., 72, 1–19, doi:10.1007/s10874-013-9265-6, 2013. 13108

Brion, J., Chakir, A., Daumont, D., Malicet, J., and Parisse, C.: High-resolution laboratory absorption cross section of O_3, Temperature effect, Chem. Phys. Lett., 213, 610–612, 1993. 13140

Bucsela, E. J., Krotkov, N. A., Celarier, E. A., Lamsal, L. N., Swartz, W. H., Bhartia, P. K., Boersma, K. F., Veefkind, J. P., Gleason, J. F., and Pickering, K. E.: A new stratospheric and tropospheric NO_2 retrieval algorithm for nadir-viewing satellite instruments: applications to OMI, Atmos. Meas. Tech., 6, 2607–2626, doi:10.5194/amt-6-2607-2013, 2013. 13102

Byun, D. and Schere, K. L.: Review of the governing equations, computational algorithms, and other components of the Models-3 Community Multiscale Air Quality (CMAQ) modeling system, Appl. Mech. Rev., 59, 51–77, doi:10.1115/1.2128636, 2006. 13109

Cai, Z., Liu, Y., Liu, X., Chance, K., Nowlan, C. R., Lang, R., Munro, R., and Suleiman, R.: Characterization and correction of global ozone monitoring experiment 2 ultraviolet measurements and application to ozone profile retrievals, J. Geophys. Res.: Atmos., 117, doi:10.1029/2011JD017096, 2012. 13111

Chance, K. and Kurucz, R. L.: An improved high-resolution solar reference spectrum for Earth's atmosphere measurements in the ultraviolet, visible, and near infrared, J. Quant. Spectrosc. Ra., 111, 1289–1295, doi:10.1016/j.jqsrt.2010.01.036, 2010. 13111, 13112

Chance, K., Palmer, P. I., Spurr, R. J., Martin, R. V., Kurosu, T. P., and Jacob, D. J.: Satellite observations of formaldehyde over North America from GOME, Geophys. Res. Lett., 27, 3461–3464, 2000. 13111

Chance, K., Kurosu, T. P., and Sioris, C. E.: Undersampling correction for array detector-based satellite spectrometers, Appl. Optics, 44, 1296–1304, doi:10.1364/AO.44.001296, 2005. 13113, 13140

Chance, K., Liu, X., Suleiman, R. M., Flittner, D. E., Al-Saadi, J., and Janz, S. J.: Tropospheric emissions: monitoring of pollution (TEMPO), Proc. SPIE 8866, Earth Observing Systems XVIII, 8866, 88660D-1–88660D-16, doi:10.1117/12.2024479, 2013. 13102, 13118

Chance, K. V. and Spurr, R. J. D.: Ring effect studies: Rayleigh scattering, including molecular parameters for rotational Raman scattering, and the Fraunhofer spectrum, Appl. Optics, 36, 5224–5230, 1997. 13140

Fishman, J., Iraci, L. T., Al-Saadi, J., Chance, K., Chavez, F., Chin, M., Coble, P., Davis, C., DiGiacomo, P. M., Edwards, D., Eldering, A., Goes, J., Herman, J., Hu, C., Jacob, D. J., Jordan, C., Kawa, S. R., Key, R., Liu, X., Lohrenz, S., Mannino, A., Natraj, V., Neil, D., Neu, J., Newchurch, M., Pickering, K., Salisbury, J., Sosik, H., Subramaniam, A., Tzortziou, M., Wang, J., and Wang, M.: The United States' next generation of atmospheric composition and coastal ecosystem measurements: NASA's geostationary coastal and air pollution events (GEO-CAPE) Mission, B. Am. Meteorol. Soc., 93, 1547–1566, doi:10.1175/bams-d-11-00201.1, 2012. 13102

Flynn, C. M., Pickering, K. E., Crawford, J. H., Lamsal, L., Krotkov, N., Herman, J., Weinheimer, A., Chen, G., Liu, X., Szykman, J., Tsay, S.-C., Loughner, C., Hains, J., Lee, P., Dickerson, R. R., Stehr, J. W., and Brent, L.: Relationship between column-density and surface mixing ratio: Statistical analysis of O_3 and NO_2 data from the July 2011 Maryland DISCOVER-AQ mission, Atmos. Environ., 92, 429–441, doi:10.1016/j.atmosenv.2014.04.041, 2014. 13124

General, S., Pöhler, D., Sihler, H., Bobrowski, N., Frieß, U., Zielcke, J., Horbanski, M., Shepson, P. B., Stirm, B. H., Simpson, W. R., Weber, K., Fischer, C., and Platt, U.: The Heidelberg Airborne Imaging DOAS Instrument (HAIDI) – a novel imaging DOAS device for 2-D and 3-D imaging of trace gases and aerosols, Atmos. Meas. Tech., 7, 3459–3485, doi:10.5194/amt-7-3459-2014, 2014. 13103

González Abad, G., Liu, X., Chance, K., Wang, H., Kurosu, T. P., and Suleiman, R.: Updated Smithsonian Astrophysical Observatory Ozone Monitoring Instrument (SAO OMI) formaldehyde retrieval, Atmos. Meas. Tech., 8, 19–32, doi:10.5194/amt-8-19-2015, 2015a. 13111

González Abad, G., Vasilkov, A., Seftor, C., Liu, X., and Chance, K.: Smithsonian Astrophysical Observatory Ozone Mapping and Profiler Suite (SAO OMPS) formaldehyde retrieval, Atmos. Meas. Tech. Discuss., 8, 9209–9240, doi:10.5194/amtd-8-9209-2015, 2015b. 13111

Hair, J. W., Hostetler, C. A., Cook, A. L., Harper, D. B., Ferrare, R. A., Mack, T. L., Welch, W., Izquierdo, L. R., and Hovis, F. E.: Airborne high spectral resolution lidar for profiling aerosol optical properties, Appl. Optics, 47, 6734–6752, doi:10.1364/AO.47.006734, 2008. 13109

Herman, J., Cede, A., Spinei, E., Mount, G., Tzortziou, M., and Abuhassan, N.: NO_2 column amounts from ground-based Pandora and MFDOAS spectrometers using the direct-sun

Title Page

Abstract | Introduction

Conclusions | References

Tables | Figures

◄◄ | ►►

◄ | ►

Back | Close

Full Screen / Esc

Printer-friendly Version

Interactive Discussion

DOAS technique: Intercomparisons and application to OMI validation, J. Geophys. Res.-Atmos., 114, D13307, doi:10.1029/2009JD011848, 2009. 13107

Heue, K.-P., Wagner, T., Broccardo, S. P., Walter, D., Piketh, S. J., Ross, K. E., Beirle, S., and Platt, U.: Direct observation of two dimensional trace gas distributions with an airborne Imaging DOAS instrument, Atmos. Chem. Phys., 8, 6707–6717, doi:10.5194/acp-8-6707-2008, 2008. 13103, 13142

Illing, R. M. E.: Design and development of the PolZero Time Domain Polarization Scrambler, roc. SPIE 7461, Polarization Science and Remote Sensing IV, 746104-1–746104–10, doi:10.1117/12.826217, 2009. 13105

Ingmann, P., Veihelmann, B., Langen, J., Lamarre, D., Stark, H., and Courrèges-Lacoste, G. B.: Requirements for the GMES atmosphere service and ESA's implementation concept: sentinels-4/-5 and-5p, Remote Sens. Environ., 120, 58–69, doi:10.1016/j.rse.2012.01.023, 2012. 13102

Kim, J.: GEMS (Geostationary Environment Monitoring Spectrometer) onboard the GeoKOMP-SAT to Monitor Air Quality in high Temporal and Spatial Resolution over Asia-Pacific Region, in: EGU General Assembly Conference Abstracts, edited by: Abbasi, A. and Giesen, N., Vol. 14, EGU General Assembly Conference Abstracts, 22–27 April 2012, Vienna, Austria, p. 4051, 2012. 13102

Kleipool, Q. L., Dobber, M. R., de Haan, J. F., and Levelt, P. F.: Earth surface reflectance climatology from 3 years of OMI data, J. Geophys. Res.-Atmos., 113, d18308, doi:10.1029/2008JD010290, 2008. 13119

Kowalewski, M. G. and Janz, S. J.: Remote sensing capabilities of the GEO-CAPE airborne simulator, Proc. SPIE, 9218, 92181I–92181I–12, doi:10.1117/12.2062058, 2014. 13103, 13109

Lamsal, L. N., Martin, R. V., Van Donkelaar, A., Steinbacher, M., Celarier, E. A., Bucsela, E., Dunlea, E. J., and Pinto, J. P.: Ground-level nitrogen dioxide concentrations inferred from the satellite-borne Ozone Monitoring Instrument, J. Geophys. Res.-Atmos., 113, D16308, doi:10.1029/2007JD009235, 2008. 13108, 13123

Lamsal, L. N., Martin, R. V., Van Donkelaar, A., Celarier, E. A., Bucsela, E. J., Boersma, K. F., Dirksen, R., Luo, C., and Wang, Y.: Indirect validation of tropospheric nitrogen dioxide retrieved from the OMI satellite instrument: Insight into the seasonal variation of nitrogen oxides at northern midlatitudes, J. Geophys. Res.-Atmos., 115, D05302, doi:10.1029/2009JD013351, 2010. 13123

NO$_2$ retrievals from GeoTASO

C. R. Nowlan et al.

Title Page

Abstract	Introduction
Conclusions	References
Tables	Figures

|◄ | ►|

◄ | ►

Back | Close

Full Screen / Esc

Printer-friendly Version

Interactive Discussion

Lamsal, L. N., Martin, R. V., Parrish, D. D., and Krotkov, N. A.: Scaling relationship for NO_2 pollution and urban population size: a satellite perspective, Environ. Sci. Technol., 47, 7855–7861, doi:10.1021/es400744g, 2013. 13102, 13123

Lamsal, L. N., Duncan, B. N., Yoshida, Y., Krotkov, N. A., Pickering, K. E., Streets, D. G., and Lu, Z.: U. S. NO_2 trends (2005–2013): EPA Air Quality System (AQS) data versus improved observations from the Ozone Monitoring Instrument (OMI), Atmos. Environ., 110, 130–143, doi:10.1016/j.atmosenv.2015.03.055, 2015. 13123

Lawrence, J. P., Anand, J. S., Vande Hey, J. D., White, J., Leigh, R. R., Monks, P. S., and Leigh, R. J.: High-resolution measurements from the airborne Atmospheric Nitrogen Dioxide Imager (ANDI), Atmos. Meas. Tech., 8, 4735–4754, doi:10.5194/amt-8-4735-2015, 2015. 13103

Leitão, J., Richter, A., Vrekoussis, M., Kokhanovsky, A., Zhang, Q. J., Beekmann, M., and Burrows, J. P.: On the improvement of NO_2 satellite retrievals – aerosol impact on the airmass factors, Atmos. Meas. Tech., 3, 475–493, doi:10.5194/amt-3-475-2010, 2010. 13119

Leitch, J. W., Delker, T., Good, W., Ruppert, L., Murcray, F., Chance, K., Liu, X., Nowlan, C., Janz, S. J., Krotkov, N. A., Pickering, K. E., Kowalewski, M., and Wang, J.: The GeoTASO airborne spectrometer project, Proc. SPIE, 9218, 92181H–92181H–9, doi:10.1117/12.2063763, 2014. 13102, 13104, 13111

Lin, J.-T., Martin, R. V., Boersma, K. F., Sneep, M., Stammes, P., Spurr, R., Wang, P., Van Roozendael, M., Clémer, K., and Irie, H.: Retrieving tropospheric nitrogen dioxide from the Ozone Monitoring Instrument: effects of aerosols, surface reflectance anisotropy, and vertical profile of nitrogen dioxide, Atmos. Chem. Phys., 14, 1441–1461, doi:10.5194/acp-14-1441-2014, 2014. 13119

Liu, C., Liu, X., Kowalewski, M. G., Janz, S. J., González Abad, G., Pickering, K. E., Chance, K., and Lamsal, L. N.: Characterization and verification of ACAM slit functions for trace-gas retrievals during the 2011 DISCOVER-AQ flight campaign, Atmos. Meas. Tech., 8, 751–759, doi:10.5194/amt-8-751-2015, 2015. 13109, 13111

Liu, X., Chance, K., Sioris, C. E., Spurr, R. J. D., Kurosu, T. P., Martin, R. V., and Newchurch, M. J.: Ozone profile and tropospheric ozone retrievals from the global ozone monitoring experiment: algorithm description and validation, J. Geophys. Res.-Atmos., 110, doi:10.1029/2005JD006240, 2005. 13111

NO_2 retrievals from GeoTASO

C. R. Nowlan et al.

Title Page

Abstract	Introduction
Conclusions	References
Tables	Figures

|◄ | ►|

◄ | ►

Back | Close

Full Screen / Esc

Printer-friendly Version

Interactive Discussion

Liu, X., Bhartia, P. K., Chance, K., Spurr, R. J. D., and Kurosu, T. P.: Ozone profile retrievals from the Ozone Monitoring Instrument, Atmos. Chem. Phys., 10, 2521–2537, doi:10.5194/acp-10-2521-2010, 2010. 13116

Martin, R. V., Chance, K., Jacob, D. J., Kurosu, T. P., Spurr, R. J., Bucsela, E., Gleason, J. F., Palmer, P. I., Bey, I., Fiore, A. M., Li, Q., Yantosca, R. M., and Koelemeijer, R. B. A.: An improved retrieval of tropospheric nitrogen dioxide from GOME, J. Geophys. Res.-Atmos., 107, ACH-9, doi:10.1029/2001JD001027, 2002. 13102, 13118

McLinden, C. A., Olsen, S. C., Hannegan, B., Wild, O., Prather, M. J., and Sundet, J.: Stratospheric ozone in 3-D models: A simple chemistry and the cross-tropopause flux, J. Geophys. Res.-Atmos., 105, 14653–14665, 2000. 13116

McLinden, C. A., Fioletov, V., Boersma, K. F., Kharol, S. K., Krotkov, N., Lamsal, L., Makar, P. A., Martin, R. V., Veefkind, J. P., and Yang, K.: Improved satellite retrievals of NO_2 and SO_2 over the Canadian oil sands and comparisons with surface measurements, Atmos. Chem. Phys., 14, 3637–3656, doi:10.5194/acp-14-3637-2014, 2014. 13123

Munro, R., Lang, R., Klaes, D., Poli, G., Retscher, C., Lindstrot, R., Huckle, R., Lacan, A., Grzegorski, M., Holdak, A., Kokhanovsky, A., Livschitz, J., and Eisinger, M.: The GOME-2 instrument on the Metop series of satellites: instrument design, calibration, and level 1 data processing – an overview, Atmos. Meas. Tech. Discuss., 8, 8645–8700, doi:10.5194/amtd-8-8645-2015, 2015. 13109

Nowlan, C. R., Liu, X., Chance, K., Cai, Z., Kurosu, T. P., Lee, C., and Martin, R. V.: Retrievals of sulfur dioxide from the global ozone monitoring experiment 2 (GOME-2) using an optimal estimation approach: algorithm and initial validation, J. Geophys. Res.-Atmos., 116, doi:10.1029/2011JD015808, 2011. 13111

Nowlan, C. R., Martin, R. V., Philip, S., Lamsal, L. N., Krotkov, N. A., Marais, E. A., Wang, S., and Zhang, Q.: Global dry deposition of nitrogen dioxide and sulfur dioxide inferred from space-based measurements, Global Biogeochem. Cy., 28, 1025–1043, doi:10.1002/2014GB004805, 2014. 13123

Otte, T. L. and Pleim, J. E.: The Meteorology–Chemistry Interface Processor (MCIP) for the CMAQ modeling system: updates through MCIPv3.4.1, Geosci. Model Dev., 3, 243–256, doi:10.5194/gmd-3-243-2010, 2010. 13109

Palmer, P. I., Jacob, D. J., Chance, K., Martin, R. V., Spurr, R. J., Kurosu, T. P., Bey, I., Yantosca, R., Fiore, A., and Li, Q.: Air mass factor formulation for spectroscopic measurements from satellites: application to formaldehyde retrievals from the global ozone monitoring ex-

NO$_2$ retrievals from GeoTASO

C. R. Nowlan et al.

Title Page

Abstract	Introduction
Conclusions	References
Tables	Figures

|◄ | ►|
◄ | ►

Back | Close

Full Screen / Esc

Printer-friendly Version

Interactive Discussion

periment, J. Geophys. Res.-Atmos., 106, 14539–14550, doi:10.1029/2000JD900772, 2001. 13115

Popp, C., Brunner, D., Damm, A., Van Roozendael, M., Fayt, C., and Buchmann, B.: High-resolution NO_2 remote sensing from the Airborne Prism EXperiment (APEX) imaging spectrometer, Atmos. Meas. Tech., 5, 2211–2225, doi:10.5194/amt-5-2211-2012, 2012. 13103, 13114

Prather, M.: Catastrophic loss of stratospheric ozone in dense volcanic clouds, J. Geophys. Res.-Atmos., 97, 10187–10191, 1992. 13116

Richter, A., Begoin, M., Hilboll, A., and Burrows, J. P.: An improved NO_2 retrieval for the GOME-2 satellite instrument, Atmos. Meas. Tech., 4, 1147–1159, doi:10.5194/amt-4-1147-2011, 2011. 13102

Román, M. O., Gatebe, C. K., Schaaf, C. B., Poudyal, R., Wang, Z., and King, M. D.: Variability in surface BRDF at different spatial scales (30–500 m) over a mixed agricultural landscape as retrieved from airborne and satellite spectral measurements, Remote Sens. Environ., 115, 2184–2203, doi:10.1016/j.rse.2011.04.012, 2011. 13119

Rothman, L., Gordon, I., Babikov, Y., Barbe, A., Chris Benner, D., Bernath, P., Birk, M., Bizzocchi, L., Boudon, V., Brown, L., Campargue, A., Chance, K., Cohen, E. A., Coudert, L., Devi, V., Drouin, B. J., Fayt, A., Flaud, J.-M., Gamache, R., Harrison, J., Hartmann, J.-M., Hill, C., Hodges, J., Jacquemart, D., Jolly, A., Lamouroux, J., Le Roy, R., Li, G., Long, D., Lyulin, O., Mackie, C., Massie, S., Mikhailenko, S., Müller, H., Naumenko, O., Nikitin, A., Orphal, J., Perevalov, V., Perrin, A., Polovtseva, E., Richard, C., Smith, M., Starikova, E., Sung, K., Tashkun, S., Tennyson, J., Toon, G., Tyuterev, V., and Wagner, G.: The HITRAN 2012 molecular spectroscopic database, J. Quant. Spectrosc. Ra., 130, 4–50, doi:10.1016/j.jqsrt.2013.07.002, 2013. 13140

Sather, M. E. and Cavender, K.: Update of long-term trends analysis of ambient 8 hour ozone and precursor monitoring data in the South Central US, encouraging news, J. Environ. Monitor., 14, 666–676, doi:10.1039/C2EM10862C, 2012. 13121

Schaaf, C. B., Gao, F., Strahler, A. H., Lucht, W., Li, X., Tsang, T., Strugnell, N. C., Zhang, X., Jin, Y., Muller, J.-P., Lewis, P., Barnsley, M., Hobson, P., Disney, M., Roberts, G., Dunderdale, M., Doll, C., d'Entremont, R. P. Hu, B., Liang, S., Privette, J. L., and Roy, D.: First operational BRDF, albedo nadir reflectance products from MODIS, Remote Sens. Environ., 83, 135–148, doi:10.1016/S0034-4257(02)00091-3, 2002. 13115

Title Page

Abstract | Introduction

Conclusions | References

Tables | Figures

|◄ | ►|

◄ | ►

Back | Close

Full Screen / Esc

Printer-friendly Version

Interactive Discussion

Schönhardt, A., Altube, P., Gerilowski, K., Krautwurst, S., Hartmann, J., Meier, A. C., Richter, A., and Burrows, J. P.: A wide field-of-view imaging DOAS instrument for continuous trace gas mapping from aircraft, Atmos. Meas. Tech. Discuss., 7, 3591–3644, doi:10.5194/amtd-7-3591-2014, 2014. 13103

Skamarock, W. C., Klemp, J. B., Dudhia, J., Gill, D. O., Barker, D. L., Duda, M. G., Huang, X.-Y., Wang, W., and Powers, J. G.: A description of the Advanced Research WRF version 3, Tech. Rep. NCAR/TN-475+STR, NCAR, Boulder, CO, 2008. 13109

Spurr, R. J.: VLIDORT: A linearized pseudo-spherical vector discrete ordinate radiative transfer code for forward model and retrieval studies in multilayer multiple scattering media, J. Quant. Spectrosc. Ra., 102, 316–342, doi:10.1016/j.jqsrt.2006.05.005, 2006. 13115

Thalman, R. and Volkamer, R.: Temperature dependent absorption cross-sections of O_2-O_2 collision pairs between 340 and 630 nm and at atmospherically relevant pressure, Phys. Chem. Chem. Phys., 15, 15371–15381, doi:10.1039/c3cp50968k, 2013. 13140

Vandaele, A. C., Hermans, C., Simon, P. C., Carleer, M., Colin, R., Fally, S., Mérienne, M. F., Jenouvrier, A., and Coquart, B.: Measurements of the NO_2 absorption cross-section from 42,000 to 10,000 cm^{-1} (238–1000 nm) at 220 and 294 K, J. Quant. Spectrosc. Ra., 59, 171–184, 1998. 13107, 13140

Wang, J.: An algorithm for simultaneous inversion of aerosol properties and surface reflectance from airborne Geo-TASO hyperspectral data, in: Fourier Transform Spectroscopy and Hyperspectral Imaging and Sounding of the Environment, p. HT3 B.6, Optical Society of America, Washington, DC, USA, doi:10.1364/HISE.2015.HT3B.6, 2015. 13121

Title Page

Abstract | Introduction

Conclusions | References

Tables | Figures

|◄ | ►|

◄ | ►

Back | Close

Full Screen / Esc

Printer-friendly Version

Interactive Discussion

Table 1. GeoTASO instrument characteristics. Four different slit sizes can be used in a slit holder assembly to give different spectral resolutions and spectral sampling values.

Characteristic	UV	VIS
Wavelength range	290–400 nm	415–695 nm
Spectral resolution in FWHM (slit size=26.0; 32.5; 39.0; 45.5 μm)	0.34; 0.39; 0.43; 0.49 nm	0.70; 0.75; 0.88; 1.00 nm
Spectral sampling per FWHM	2.5; 2.8; 3.1; 3.5 pixels	2.5; 2.7; 3.1; 3.6 pixels
Full cross-track field-of-view	45°	
Single frame cross-track field-of-view	0.046°	
Single frame spatial resolution at ground	9 m × 50 m with aircraft at 11 km, speed = 200 m s^{-1}, pitch = 0°	

Table 2. Summary of GeoTASO flights during Discover-AQ Texas 2013. LT = UTC − 4 h for 12 September and LT = UTC − 5 h for other days.

Date	Flight Summary	Flight Time (LT)	Slit size (µm)
12 September	Flight to Houston from Virginia	14:37–17:50	39.0
13 September	Houston	08:20–11:34	39.0
14 September	Houston	13:48–17:06	32.5
16 September	OMI satellite underpass, Oklahoma	13:15–15:46	39.0
17 September	Boat and water overpasses	08:35–10:27	45.5
18 September	Houston	09:01–12:06	26.0
24 September	Leg 1: Houston	10:07–12:08	45.5
	Leg 2: Flight to Virginia, power plant overpasses	14:10–16:16	45.5

Table 3. DISCOVER-AQ sites used in GeoTASO validation and site instrumentation. The Pandora ID is a identification number given to each individual Pandora instrument.

Site	Latitude (°)	Longitude (°)	Pandora ID	In Situ Instrument
Channelview	29.803	−95.126	P26	TCEQ FRM
Conroe	30.350	−95.425	P31	TCEQ FRM
Deer Park	29.670	−95.128	P32	TCEQ FRM
Galveston	29.254	−94.861	P34	photolytic, TCEQ FRM
Harris	30.039	−95.674	P30	TCEQ FRM
La Porte	29.672	−95.065	P38, P39	CAPS, EPA FRM
Manvel Croix	29.520	−95.392	P33	CRD, TCEQ FRM
Moody Tower	29.718	−95.341	P28, P35	photolytic
Seabrook Park	29.901	−95.326	P27	photolytic, TCEQ FRM
Smith Point	29.546	−94.787	P8, P29, P36	CAPS
Texas Avenue	29.753	−95.350		photolytic, TCEQ FRM
West Houston	29.833	−95.657	P18	

Table 4. WRF and CMAQ model options.

Weather Research and Forecasting (WRF) Version 3.6.1 Model Options	
Radiation	LW: RRTM; SW: Goddard
Surface layer	Pleim-Xiu
Land surface model	Pleim-Xiu
Boundary layer	ACM2
Cumulus	Kain-Fritsch
Microphysics	WSM-6
Nudging	Observational and analysis nudging
Damping	Vertical velocity and gravity waves damped at top of modeling domain
SSTs	Multi-scale Ultra-high Resolution (MUR) SST analysis (1 km resolution)
CMAQ Version 5.0.2 Model Options	
Chemical mechanism	CB05
Aerosols	AE5
Dry deposition	M3DRY
Vertical diffusion	ACM2
Emissions	2012 TCEQ anthropogenic emissions
	Biogenic (BEIS) and lightning emissions calculated within CMAQ
Initial and boundary conditions	MOZART CTM

Table 5. Reference cross sections and parameters fit in NO$_2$ retrieval.

Parameter	Note
NO$_2$	Vandaele et al. (1998), 294 K
O$_3$	Brion et al. (1993), 218 and 295 K
H$_2$O vapor	Rothman et al. (2013), 288 K, 1 atm
O$_2$–O$_2$	Thalman and Volkamer (2013), 293 K
Ring spectrum	Chance and Spurr (1997)
Undersampling	Chance et al. (2005)
Baseline polynomial	4th order
Scaling polynomial	5th order
Wavelength shift	
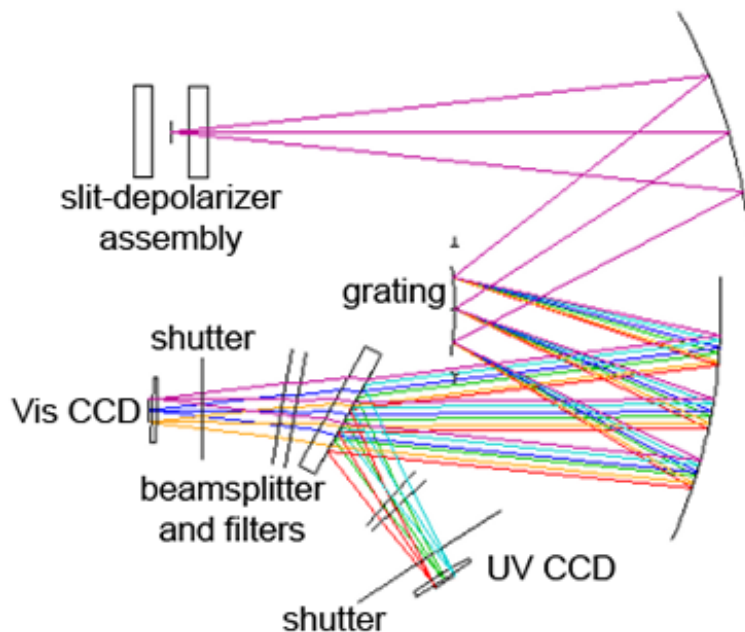
Figure 1. GeoTASO spectrometer design. First and second diffraction orders are separated into Vis and UV channels by the beamsplitter and filters.

Full Screen / Esc
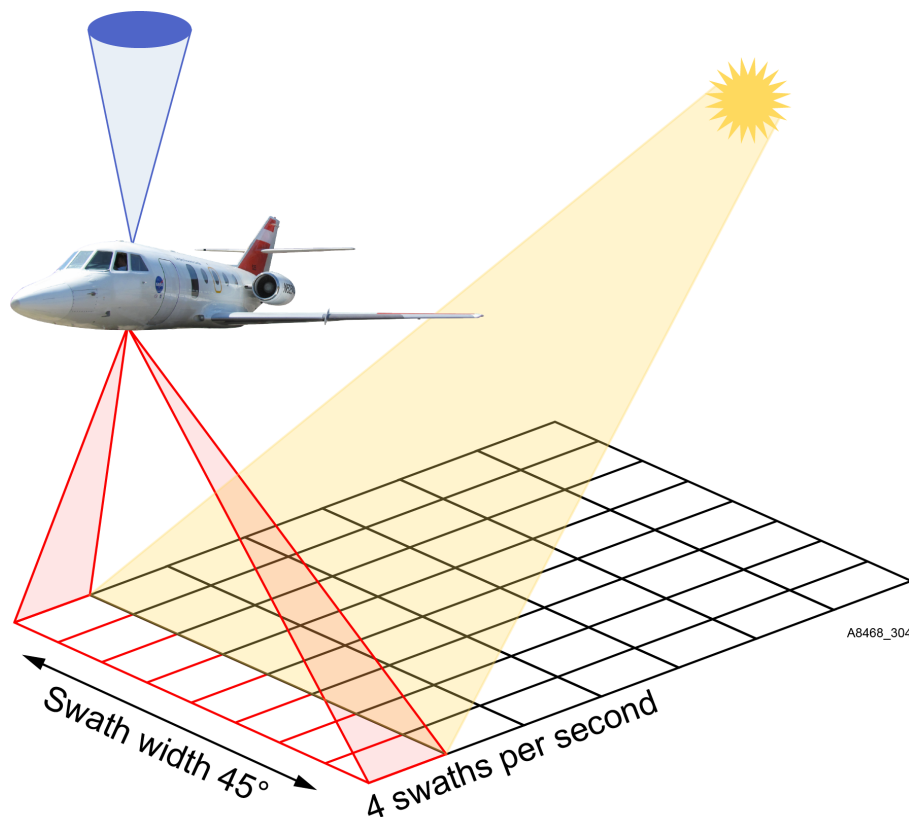
Figure 2. Schematic of GeoTASO measurement approach. The nadir observations are shown in red and zenith sky view in blue. In practice, there are approximately 975 spatial samples across the swath (after Heue et al., 2008).

A8468_304

Swath width 45°

4 swaths per second
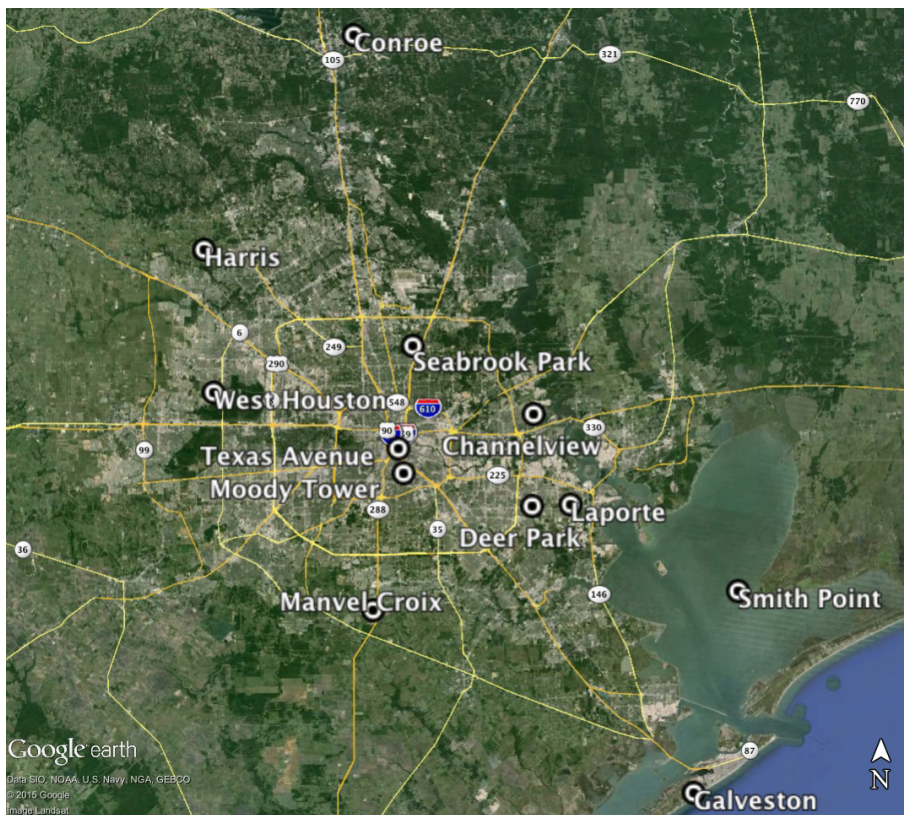
Figure 3. Location of ground sites in Houston area during DISCOVER-AQ 2013. Major roads are shown in yellow.
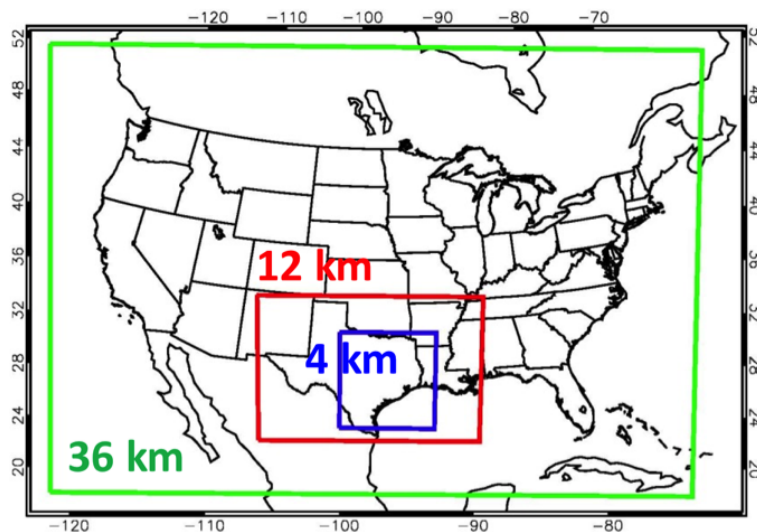
Figure 4. 36, 12, and 4 km CMAQ modeling domains.

Full Screen / Esc

Printer-friendly Version

Interactive Discussion
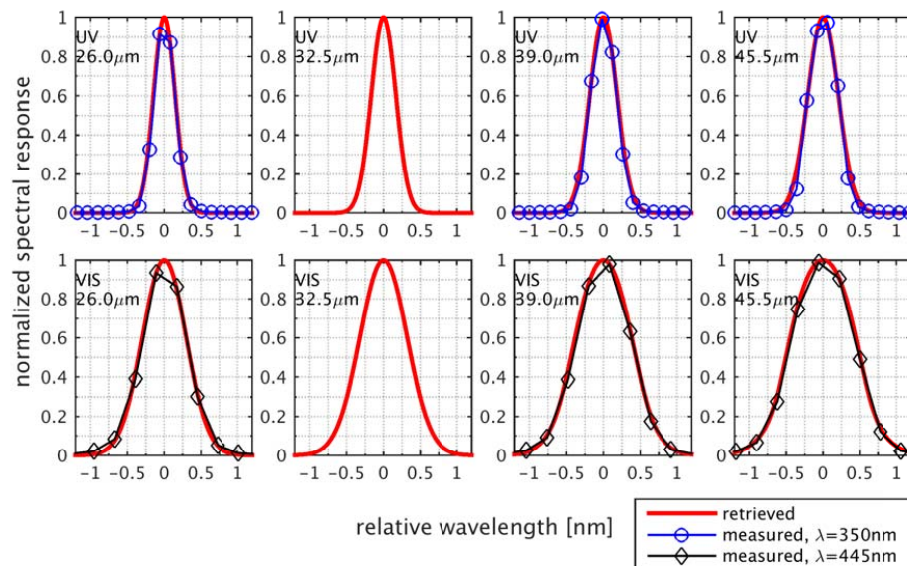
Figure 5. Slit function shapes retrieved from nadir radiance data for UV and VIS spectrometers and those recorded post-flight in the laboratory at 350 and 445 nm for the center FOV position. Data were not collected in the laboratory for the 32.5 μm slit due to time constraints. Data for the 39 μm slit are shown at 440 nm, as 445 nm was not recorded.
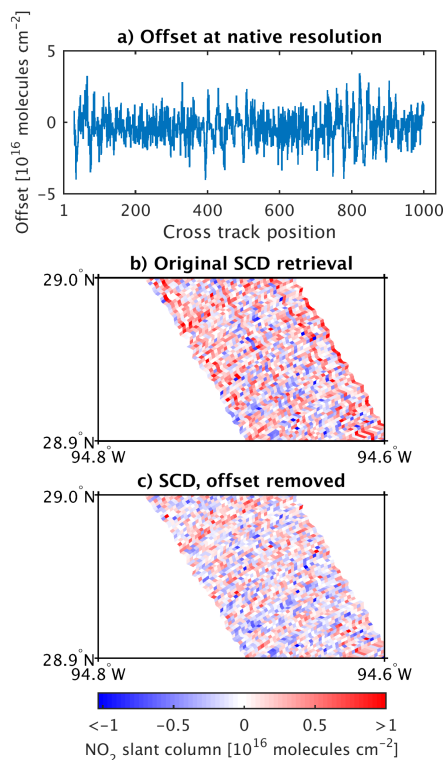
Figure 6. (a) Mean NO$_2$ slant column density (SCD) as a function of cross track position for retrievals at native spatial resolution derived from one million spectra on 13 September 2014 over a relatively clean area in the Gulf of Mexico; **(b)** Original co-added slant column retrieval at 250 m × 250 m without cross-track striping correction; and **(c)** Co-added slant column density at 250 m × 250 m corrected for cross track striping.
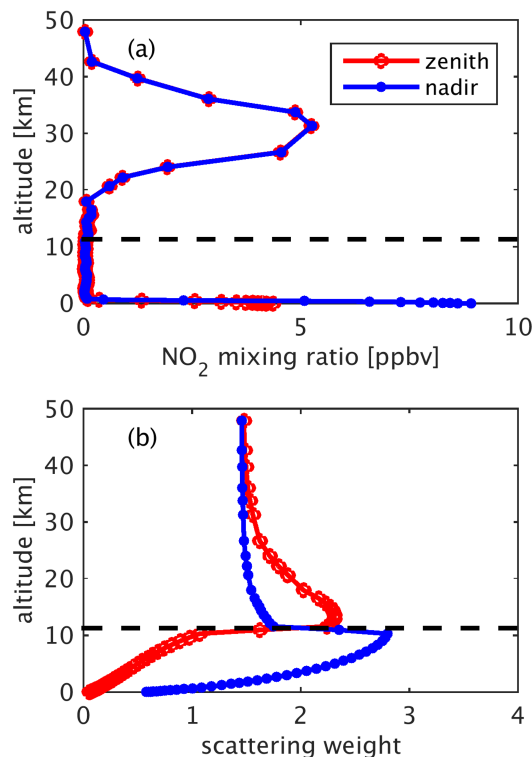
Figure 7. Sample profiles used in AMF calculation for a polluted region on 13 September 2013 10:31 LT at 29.51° N and 95.34° W, SZA = 47.0°, VZA = 13.2° showing **(a)** modeled NO_2 mixing ratio profiles for a nadir observation and a nearby zenith observation; and **(b)** their corresponding scattering weights. The aircraft flight altitude is shown by the black dashed line. The modeled tropospheric NO_2 column is 1.1×10^{16} molecules cm^{-2} and the retrieved is 2.1×10^{16} molecules cm^{-2}.

a) 13 Sept 2013, 09:15–10:20 LT
b) 13 Sept 2013, 10:20–11:30 LT
c) 14 Sept 2013, 14:00–15:30 LT
d) 14 Sept 2013, 15:30–16:50 LT
e) 18 Sept 2013, 09:20–10:40 LT
f) 18 Sept 2013, 10:40–12:00 LT
g) 24 Sept 2013, 10:10–12:00 LT

NO$_2$ vertical column [10^{16} molecules cm^{-2}]
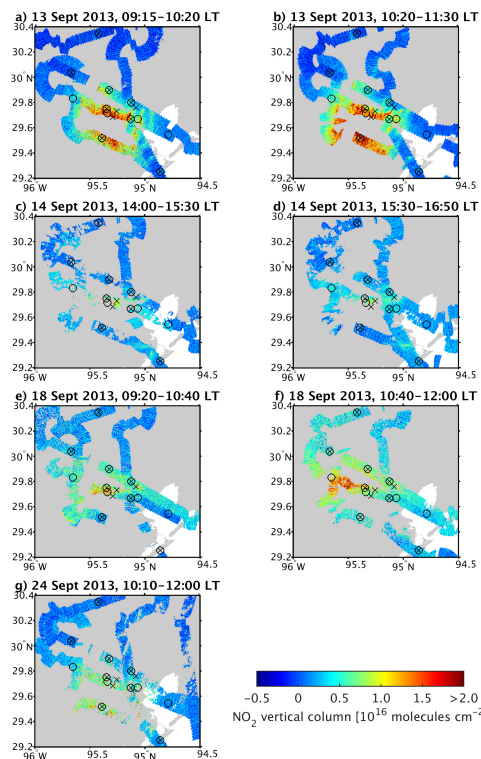
Figure 8. GeoTASO NO$_2$ tropospheric vertical columns at 250 m × 250 m resolution with precision of 2.2×10^{15} molecules cm^{-2}, retrieved for cloud-free observations over Houston during the DISCOVER-AQ campaign. Columns determined from less than 20 co-added native pixels (uncertainty $> 5 \times 10^{15}$ molecules cm^{-2}) are excluded. Locations of DISCOVER-AQ science ground sites are shown with black circles and locations of TCEQ SLAMS in situ monitors are shown with black crosses.

Title Page

Abstract | Introduction

Conclusions | References

Tables | Figures

|◄ | ►|

◄ | ►

Back | Close

Full Screen / Esc

Printer-friendly Version

Interactive Discussion
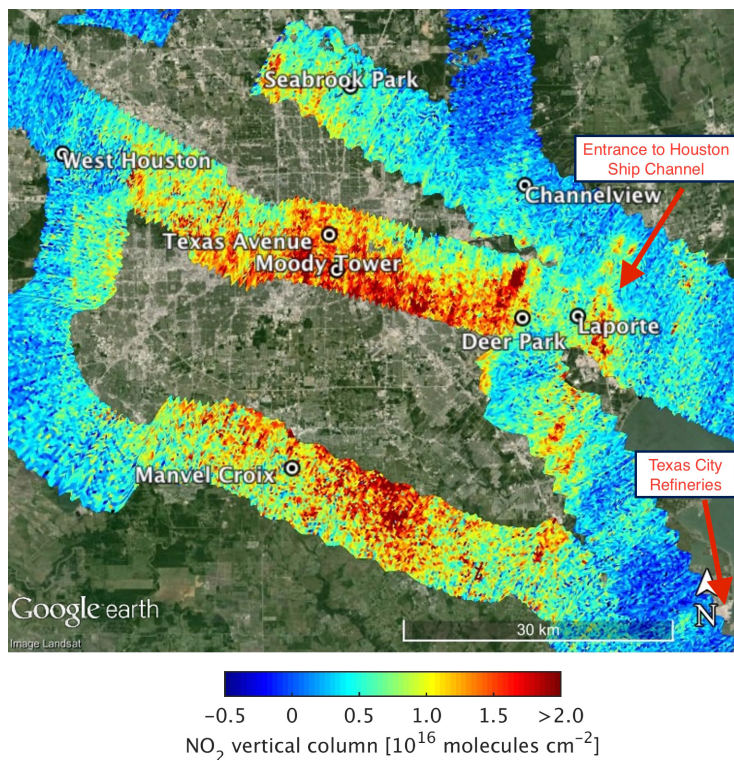
Figure 9. Enlarged view of Fig. 8a showing GeoTASO NO$_2$ tropospheric vertical columns during first Houston overpass on 13 September 2013 and DISCOVER-AQ ground stations in center of measurement region. The wave-like pattern in geolocation along the flight track is due to changes in instrument pointing from aircraft roll.
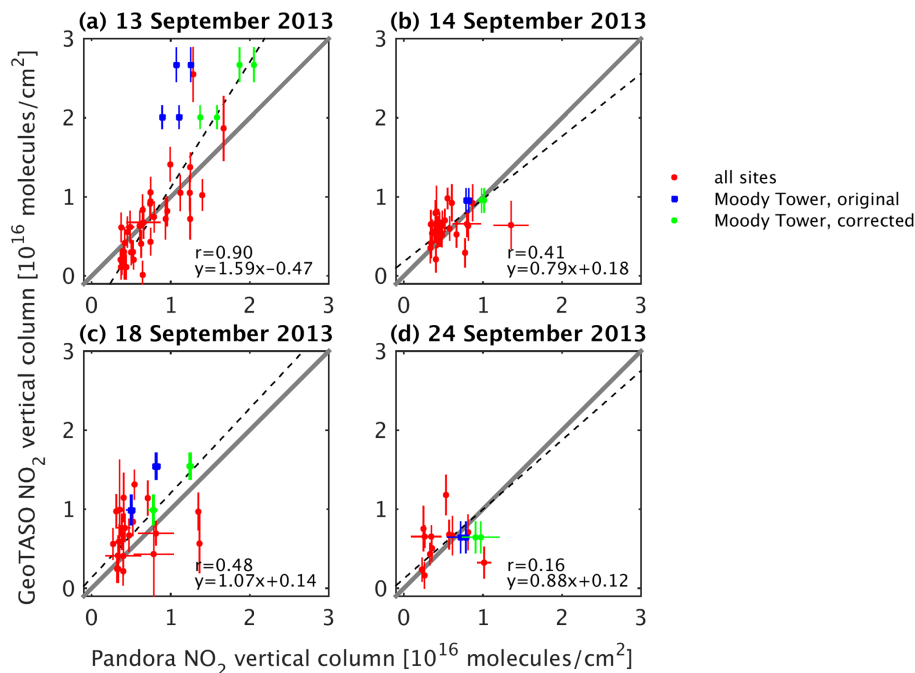
Figure 10. Pandora NO$_2$ vertical columns versus GeoTASO NO$_2$ total vertical columns (retrieved tropospheric column plus modeled stratospheric column) for cloud-free observations during four Houston urban flights during DISCOVER-AQ 2013. Data collected at the Moody Tower site (70 m) have been corrected for the partial NO$_2$ column below the tower (see text). GeoTASO error bars represent fitting uncertainties. The gray solid line represents the 1:1 ratio. The black dashed line represents a reduced major axis linear regression using all sites, including corrected Moody Tower data.

Title Page

Abstract | Introduction

Conclusions | References

Tables | Figures

◄ | ►►

◄ | ►

Back | Close

Full Screen / Esc

Printer-friendly Version

Interactive Discussion

NO$_2$ retrievals from GeoTASO
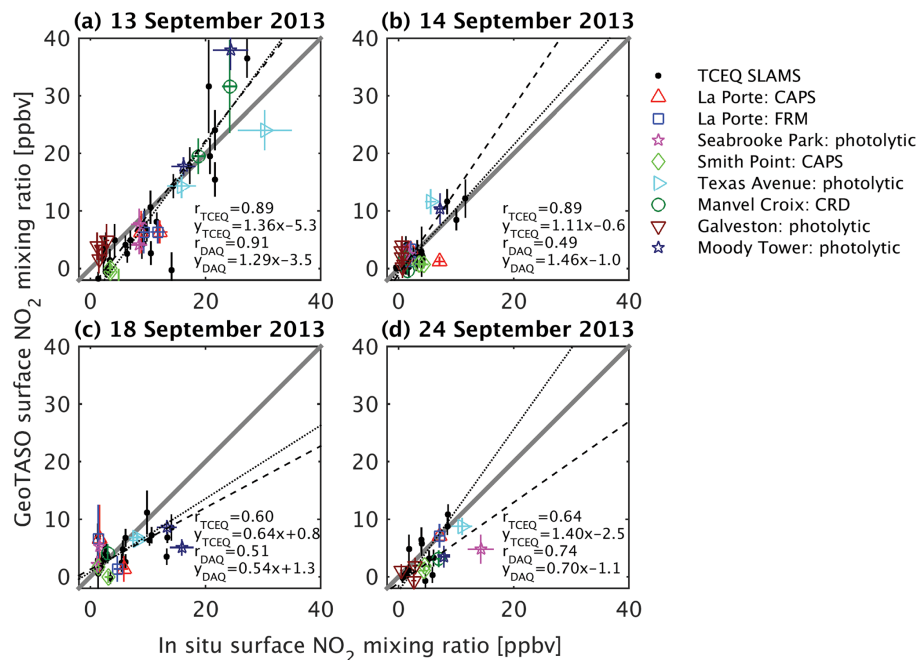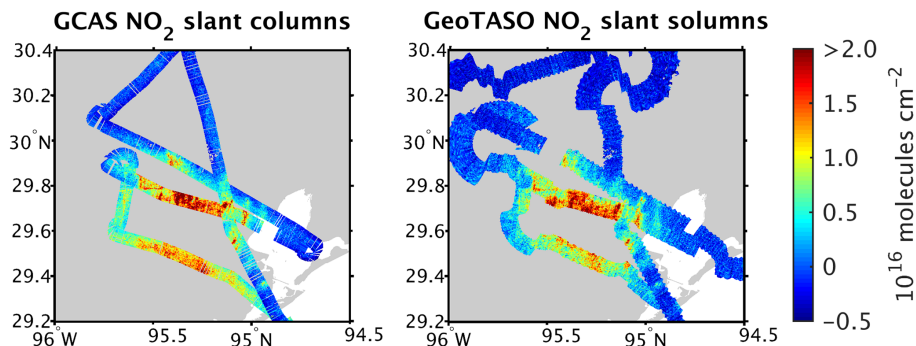
C. R. Nowlan et al.

Figure 11. In situ surface NO$_2$ mixing ratios from the TCEQ SLAMS network and DISCOVER-AQ campaign research instrumentation versus inferred surface NO$_2$ mixing ratios from Geo-TASO for cloud-free observations during four Houston urban flights during DISCOVER-AQ 2013. Correlation coefficients and regression results are shown for TCEQ monitors (TCEQ) and for the CAPS, photolytic converter and CRD monitors deployed during DISCOVER-AQ (DAQ). GeoTASO error bars represent fitting uncertainties. The gray line represents the 1:1 ratio. The black dashed (DISCOVER-AQ sites) and black dotted (TCEQ SLAMS) lines represent reduced major axis linear regressions.

Figure 12. GCAS and GeoTASO NO$_2$ retrieved slant columns at $250\,\text{m} \times 500\,\text{m}$ resolution during their first Houston overpasses on 13 September 2013 between 9:00–10:20 LT (LT = UTC − 5 h).
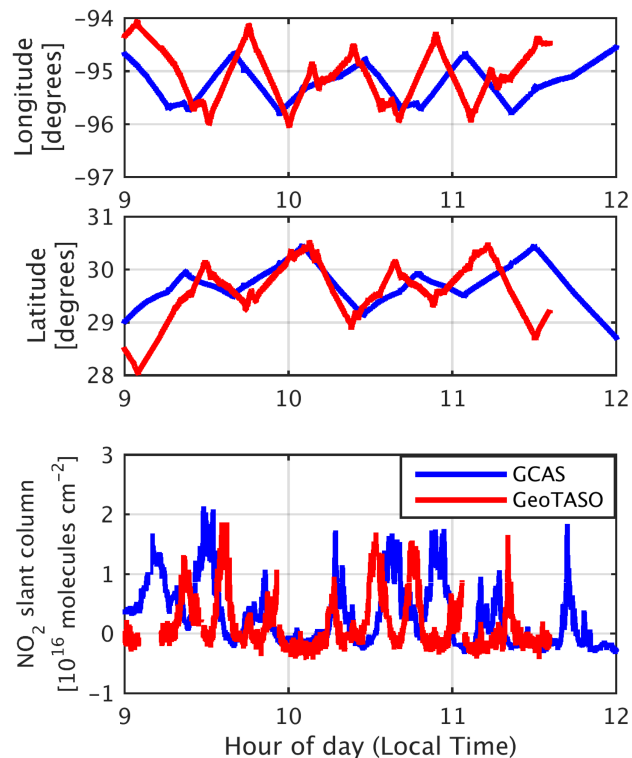
Figure 13. GCAS and GeoTASO **(a)** longitude; **(b)** latitude; and **(c)** retrieved NO$_2$ slant column as a function of time during the two morning 13 September 2013 Houston overpasses.

Title Page

Abstract | Introduction

Conclusions | References

Tables | Figures

◀ | ▶

◀ | ▶

Back | Close

Full Screen / Esc
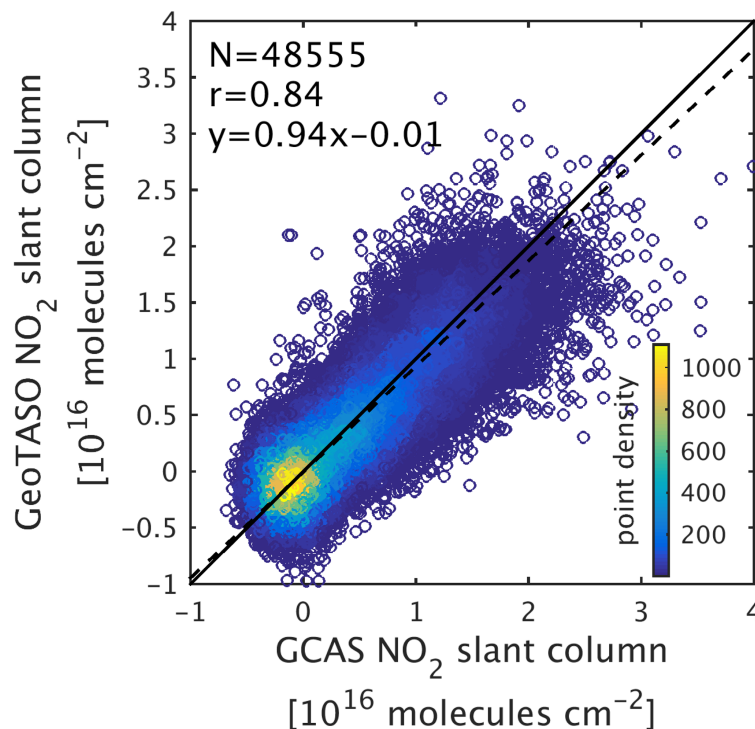
Printer-friendly Version

Interactive Discussion

Figure 14. GCAS vs. GeoTASO retrieved NO$_2$ slant columns during the two morning 13 September 2013 Houston overpasses for nearest coincident observations within 10 min and 500 m. The black solid line represents the 1 : 1 ratio. The black dashed line represents a reduced major axis linear regression.
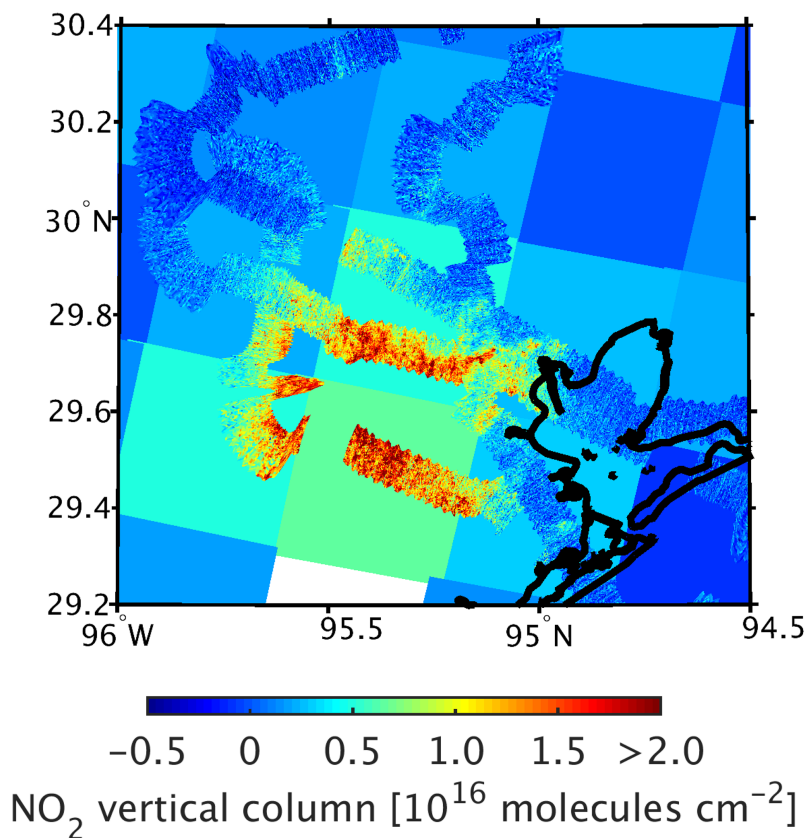
Title Page

Abstract | Introduction

Conclusions | References

Tables | Figures

|◄ | ►|

◄ | ►

Back | Close

Full Screen / Esc

Printer-friendly Version

Interactive Discussion

Figure 15. GeoTASO NO$_2$ tropospheric vertical columns at 250 m × 250 m resolution from 10:20–11:30 LT, retrieved for cloud-free observations on 13 September plotted over GOME-2/Metop-A tropospheric vertical columns where radiative cloud fraction is less than 0.5.